DYNAMIC STALL CHARACTERISTICS OF PITCHING FINITE-ASPECT-RATIO WINGS

A Dissertation
Submitted to the Graduate Faculty
of the
North Dakota State University
of Agriculture and Applied Science

By

Al Habib Ullah

In Partial Fulfillment of the Requirements
For the Degree of
DOCTOR OF PHILOSOPHY

Major Department:
Mechanical Engineering

November 2021

Fargo, North Dakota

North Dakota State University
Graduate School

Title

DYNAMIC STALL CHARACTERISTICS OF PITCHING FINITE-ASPECT-RATIO WINGS

By

Al Habib Ullah

The Supervisory Committee certifies that this *disquisition* complies with North Dakota State

University's regulations and meets the accepted standards for the degree of

DOCTOR OF PHILOSOPHY (PH.D.)

SUPERVISORY COMMITTEE:

Dr. Jordi Estevadeordal

Chair

Dr. Bora Suzen

Dr. Yan Zhang

Dr. Friedrich Littmann

Approved:

November 16, 2021	Dr. Alan Kallmeyer
Date	Department Chair

ABSTRACT

In this study, an experimental investigation was performed to characterize the dynamic stall of pitching wings and provide confirmation of the existence of the arch-shaped vortex for moderate sweep wing. Dynamic stall is a complex flow, which happens because of a sudden change of incident angle during the pitching motion. The pitching motion of a wing can cause instability in the shear layer and generate the separation burst at certain angles. For a pitching wing, the dynamic stall vortex is characterized by the formation of an arch-shaped vortex to the evolution of a ring-shaped vortex. The leg of the arch-shaped vortex causes a negative pressure region on the airfoil surface and can, in fact, generate greater lift. However, in certain conditions, the detachment of the arch-shaped vortex from the airfoil surface can cause high pressure and vibration in the structures. The formation of the arch-shaped vortex and its evolution were systematically investigated using cutting-edge flow diagnostic techniques, and the physics of the dynamic stall is explained in addition to providing the confirmation of the theory developed based on Computational Fluid Dynamics.

The study was done using Particle Image Velocimetry (PIV) and Pressure-Sensitive Paint for three sweep angle wings. The wings, with an aspect ratio of AR=4 and a NACA 0012 section assembled with round-tip, are considered for the current experimental study. The sweep angles $\Lambda= 0^0$, 15^0, and 30^0 were considered to compare the flow phenomena. The PIV results show the formation of a laminar separation bubble and its evolution to a dynamic stall vortex. The increase of sweep angle causes the formation of such vortices towards the wing tip. In the process of finding the footprint of the vortices and pressure distribution on the surface of the wings, a single-shot lifetime method using fast porous paint was used. The results show the existence of suction pressure and later grows towards the trailing edge of the wing due to the formation of a dynamic

stall vortex. In addition, at $Re=2x10^5$ and reduced frequency $k=0.2$, a moderate sweep airfoil shows the apparent footprint of the arch-shaped vortex, which confirms the current theory.

ACKNOWLEDGEMENTS

It is impossible to express in words how much support and care I have received over the last five years during my PhD. I am incredibly blessed to be surrounded by amazing people. They made my PhD journey much more straightforward.

I want to thank my thesis committee member: Dr. Yildirim Bora Suzen, Dr. Yan Zhang, and Dr. Friedrich Littmann for taking their time and teaching courses and all the exciting topics in graduate courses. I appreciate their effort. I have learned a lot from them during my tenure as a graduate student. Furthermore, I am always grateful to Dr. Yildirim Bora Suzen and Dr. Yan Zhang for giving me the opportunity to work and collaborate on many research topics.

I want to thank Dr. Jordi Estevadeordal for being a fantastic mentor, advisor, and role model. He has dedicated a lot of his valuable time teaching me all the state-of-the-art measurement techniques. His constant support helped to accomplish many projects more than I can think of. I learned countless topics and research directions in thermo-fluid science. He has shown amazing leadership in our research group and at NDSU Mechanical Engineering Department. For many numerous reasons, I could not ask for a better advisor. I also want to say that his knowledge and work will always have an imprint on my future career.

I also would like to thank our department head Dr. Alan Kallmeyer, and graduate coordinator Dr. Ghodrat Karami and Dr. Yechun Wang for taking time during my study to answer questions related to course work, research, and degree requirement, and especially to Dr. Alan

Kallmeyer for making it possible to obtain teaching experience. Without their support, I would not be able to have such a fantastic experience.

I also want to thank all the colleagues whom I worked with during my tenure as a graduate student. I have to mention Kristopher Ladd Tomek, Bailey Carlson, Charles Fabijanic, William Refling, Ruihang Zhang, Jiaming Zhao, Nick Thomas, Thomas Sprengeler, Porter Dixon, and Joshua Yurek. They have helped me in many stages during my PhD study. The works have been easier because I was always surrounded by these amazing colleagues. I have learned a lot of techniques from them, which helped to finish my project. In addition, I have to thank numerous undergraduate students who helped us in the lab to build various test setups.

I want to thank my family, especially my parents, who supported me throughout my life. My parents are the reason for who I am today and for getting my higher education. I will always be thankful to them for sacrificing everything to provide me with better education and make me the person I am today. I also want to thank my father and mother-in-law. They have been nothing but supportive over the last one year. I will always be in debt to them to support me through all the turbulence I have faced over the last year.

Lastly, I would like to thank my wife. She supported me through and through in everything. She has always been the rock in my life whom I can rely on. She knows perfect words and things to say when I have anxieties. She has been a constant motivation and support for me in the entire journey. I will never be able to thank her enough, but I will always try to do it rest of our lives.

DEDICATION

Dedicated to my parents and wife for all their love and encouragement throughout the long

journey of my PhD.

TABLE OF CONTENTS

LIST OF TABLES

LIST OF FIGURES

LIST OF ABBREVIATIONS

PIV .... Particle Image Velocimetry

LE .... Leading Edge

TE .... Trailing Edge

POD .... Proper Orthogonal Decomposition

LSB .... Laminar Separation Bubble

DSV .... Dynamic Stall Vortex

TV .... Tip Vortex

PSP .... Pressure Sensitive Paint

2D .... Two Dimensional

3D .... Three Dimensional

Ma .... Mach Number

Re .... Reynolds Number

LIST OF SYMBOLS

k ………………………………………….. Reduced Frequency

f ………………………………………….. Frequency

U ………………………………………….. Freestream Velocity

t ………………………………………….. Time

Λ ………………………………………….. Sweep Angle

ω ………………………………………….. Vorticity

V* ………………………………………….. Nondimensional Velocity

CHAPTER 1. INTRODUCTION

Purpose

This study aims to investigate the various aspects of dynamic stall associated with pitching finite-aspect ratio wing. Dynamic stall is a complex flow phenomenon, which has yet to be understood completely. As a result, this thwarts the use of pitching airfoil in myriad engineering applications despite having its aerodynamic efficiency compared to a static airfoil. To reveal the physics of the dynamic stall, various computation study has been reported. However, there is still room for findings of dynamic stall, primarily through experimental investigation. Therefore, advanced flow diagnostic methods such as the planner and 3-dimensional Particle Image Velocimetry (PIV), a fast pressure-sensitive paint, have been deployed to find dynamic stall behavior and its relation with moderate sweep angle and its evolution with different flow parameters. The current study will discuss the findings and provide the validation of the recent ongoing computation study.

Thesis Outline

In this thesis, chapter one provides the background of the study that has been conducted. Then chapter two provides the study of dynamics stall and its relation with sweep angle using PIV study. The chapter also explains the phase coherence of the flow from cycle to cycle during the pitching motion. The phase coherence is explained using Proper Orthogonal Decomposition (POD). In the next chapter, a single shot lifetime method explains the surface pressure footprint of the vortical structure associated with the dynamic stall. Chapter 3 discusses the pressure distribution on the airfoil surface using fast pressure sensitive paint technique. A fast-Porous Pressure-Sensitive Paint (PSP), which has a high response (>10 kHz), was used in the experiment. Later, the PSP technique was deployed to show a clear sign of arch vortex for moderate sweep

angle when the airfoil's pitching frequency becomes high. The finding motivates to investigate further about sweep 15-degree airfoil to perform an experiment that shows more definitive proof of arch vortex in the dynamic stall process.

CHAPTER 2. BACKGROUND

Airfoil experiencing abrupt changes in incidence angle during pitching motion is prompt to unsteady separation and dynamic stall that produces large-scale dynamic stall vortex (DSV) phenomena, notably lift and load variations [1-16]. These phenomena have also been observed in the modern application of swept-wing [1-4]. The sudden and undesirable change of wind load can have an adverse effect on controllability, structural integrity, and noise generation and therefore are essential in many engineering applications such as those involving helicopter rotors, wind turbines, wing-gust encounters, and in the maneuvering of unmanned aerial vehicle and aircraft systems [1, 2]. The advantages of swept wings in engineering applications are stability, low perturbation velocity at small Mach number, and prolonged critical value of pressure coefficient [3, 4]. It is thus essential to investigate the dynamic stall propagation for a moderate sweep wing with pitching motions.

A review of the dynamic stall has been reported in several studies including those of McCroskey [5], Carr [6], Ericsson, and Reding [7], Visbal [8], Ekaterinaris and Platzer [9], Carr and Chadrasekhara [10], etc. The fundamental understanding of the flow during DSV phenomena requires an assessment of the DSV genesis, structure, and evolution. This is especially challenging during abrupt flow incidence angle variations, such as those occurring during pitching motions. Such fundamental structure and evolution have been reported in the studies by Visbal and Garmann [1]. The study reported vortex structures and their evolution, including arch vortex, vortex ring, and tip vortices, and their formation and interactions were captured and explained through vortex phenomena such as vortex reconnection using high fidelity numerical simulations. Although the dynamics stall characteristics have been extensively reported by many studies [1, 11-13, 17], further detail about complex 3D unsteady flow remains to be explored experimentally.

3

Experiments on the dynamics stall of moderate sweep airfoil have been reported by many studies [18-22]. A very early study conducted by St. Hilaire et al. [18] found the delay of the stall with an increase in a moderate sweep of a wing and an increase in pitching frequency contribute to the rise of unsteady lift component in addition to its mean value for both swept and unswept airfoil. The aforementioned findings are also in agreement with the experiment of pressure tap measurements by Lorber et al. [19]. The pressure shows that the increase of sweep reduces the interaction of wing tip vortex with a wing, which helps to reduce the delay of the stall. Recent studies [21, 23, 24] found the existence of leading-edge vortex (LEV) on finite aspect ratio wing. The LEV grows towards the wing root for unswept or very less sweep angle. As the sweep angle increases, the LEV grows towards the wing tip, and the effect of wing tip vortex becomes minute, similar to very early studies. These experimental studies were performed with pitching axis parallel to the sweep and at low Re number with varying reduced frequency. In addition to the experimental effort, computational methods have made a significant advancement to obtaining comprehensive characteristics of the dynamic stall and the effect of sweep angle at high Re number. The process of dynamics stall was studied in detail by means of high-fidelity large-eddy simulations (LES) for the case of the ramp and sinusoidal pitching airfoil [1, 2, 8, 11, 13, 17]. For chord-based Reynolds number $Re_c=2x10^5$ and $5x10^5$, these studies also found the existence of a laminar separation bubble (LSB) in the boundary layer, which broke beyond a critical incidence. Abrupt turbulent separation formation preceded by LSB bursting was observed from the computational results. Visbal and Garman [25, 26] also investigated the dynamic stall process over pitching three-dimensional (3D) swept wing with AR=4 employing high-order LES. The flow over NACA 0012 wing with a rounded section and freestream Mach number 0.1 and with a nominal reduced frequency of 0.2 was computed. The results indicated that a DSV emerged after LSB bursting in a process that

produced an arch-shape vortex. As the pitching motion continued, the arch vortex shed into ring shape vortex via vortex reconnection as the arch vortex legs separate from the surface. The footprint of these arch vortex legs on the surface pressure was reported by Visbal and Garmann [1] for unswept and moderate wing sweep angles. They showed that the formation and evolution of DSV in the shape of an arch vortex and later shedding of ring vortex migrated towards the tip as the sweep angle increased. Few experimental efforts have been made recently Ullah and Tomek et al. [15, 16] and Rockwood et al. [27] to match the computational results from Visbal and Garman [1]. Tomek et al. and Ullah et al. [15, 16] experimented with chord-based Re=$2x10^5$ with a high pitching frequency of 33Hz that corresponds to reduced frequency k=0.2 and matches precisely with computation condition reported by that study [1]. A more robust design is implemented here to more precisely replicate the numerical simulation flow for a given phase (angle of incidence) and pitching direction (up/down). A robust pitching mechanism and phase detection (angle of incidence) was designed to allow consistent (repeatable) flow synchronization at each incidence angle and pitching direction with the data acquisition (phase-locking). This effort would also enable us to assess the phase coherence and randomness of the flow by observing instantaneous velocity, average velocity, and standard deviation at a specific phase angle and pitching cycle.

It is clear from the earlier discussion is that accurate prediction of stall and pitching moment due to wind load on the airfoil surface is crucial for lower cost and efficient operation in many aerodynamic applications. Modern diagnosis methods of pressure-sensitive paints [28, 29], capable of fine spatial resolution with high-frequency response (lifetime methods), are important to describe the unsteady aerodynamic effect to characterize the dynamic load during the pitching cycle for moderate sweep wing on pressure distribution of the unswept and moderate sweep wings. In recent years, the unsteady PSP has been applied in explaining dynamic and static-stall in

practical applications such as helicopter rotor blades, unmanned aircraft, and wind turbines in compressible [30] and incompressible [31] flow regime. In recent years PSP measurement is mostly done in the compressible flow (Mach number>0.3) regimes by many studies where pressure-sensitive paint signals can be readily detected. Some studies have successfully obtained data for incompressible and lower pressure-sensitive paint signal by averaging a large number of sample images with higher camera exposure [31, 32]. Using a large number of samples, the obtained pressure map provides a phase-average pressure map at specific phase angles [32][17]. Due to the nature of the aperiodicity of flow associated with the pitching airfoil, it is difficult to obtain the 3D vortex structure's instant footprint as reported in the computational study [1]. A single short lifetime method with high-power, short duration laser can provide enough signal to capture an instant pressure map at a specific phase angle. Phase-averages can be obtained for the phases but the level of flow repeatability or phase-coherence dictates the instantaneous-average correlation [16]. Watkins et al. [33] and Wong et al. [34] reported that lifetime based method provides a good scope of data compared to an intensity-based method. Later Watkins et al. [33] and Wong et al. [29] applied the lifetime method on the rotor blade and blade tip to measure the pressure on the wing surface.

Therefore, in this study, an experimental process and results will be reported to describe the dynamic stall of pitching airfoil. In the first part of the study, a particle image velocimetry (PIV) was conducted to obtain insight of flow structure and a fast pressure sensitive paint to obtain the surface pressure footprint of stall vortex. In addition, from the instantaneous velocity and pressure samples, phase-average and standard deviation are shown to understand how the flow and pressure structure varies from cycle-to-cycle during the pitching motion.

CHAPTER 3. PIV STUDY OF DYNAMIC STALL AND THE EFFECT OF SWEEP ON A PITCHING FINITE-ASPECT-RATIO WING

Chapter Abstract

An experimental investigation of moderate sweep on three-dimensional dynamic stall of a pitching finite-aspect ratio wing was conducted by Particle Image Velocimetry (PIV). The wings, with an aspect ratio of AR=4 and a NACA 0012 section assembled with round-tip, are 3D printed for the PIV experiment. The sweep angles Λ= 0^0, 15^0, and 30^0 were considered to compare the flow phenomena. The freestream Mach numbers, M∞=0.05 and 0.1, and the Reynolds numbers based on chord length Re_c=1x10^5 and 2x10^5 were considered as flow parameters for comparison. The airfoil pitching motion is sinusoidal and experimental values of reduced frequency were k=πfc⁄U=0.2 and 0.1, and the minimum and maximum angle of attack of pitching motion were 40 and 220, respectively. Details of flow structures for each swept case were captured at various phase angles using planar two-dimensional (2D) PIV at three spans, y/c=0.5, 0.75, and 1.0. The results obtained from the experiment show how flow starts to separate as the phase angle increases, and that the downstroke ($\downarrow$) phase angles tend to be more random and unsteady compared to upstroke ($\uparrow$) phases. As the sweep angle increases, the main separation vortex shifts towards the wing tip, and further expansion of sweep to 30^0 delays the stall compare to 0^0 and 15^0. As the Re number increases, lower reduced frequency causes dynamic stall earlier than low Re and higher reduced frequency. The results are consistent with the numerical simulations of Visbal and Garmann [1].

Experimental Setup of PIV Campaign

Wind Tunnel

The data collected for this investigation was captured using a FloTek 1440 wind tunnel which is shown in Figure 1. The wind tunnel is capable of delivering a consistent free stream

velocity of $U_\infty = 36$ m/s and the throat has dimensions of 12" x 12". This simple wind tunnel is capable of recreating flow conditions in the computational experiments.
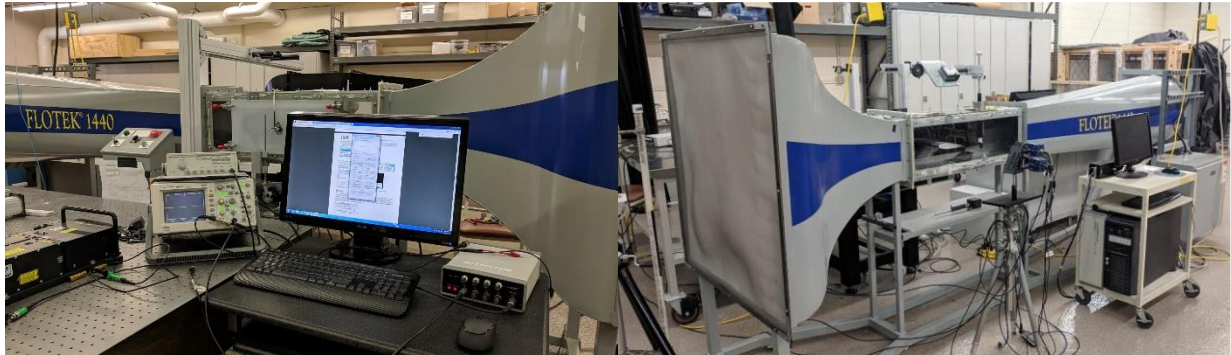
Figure 1. NDSU's FloTek 1440 wind tunnel and workstation.

Pitching Airfoil Setup

To replicate the pitching motion of the airfoil that is demonstrated in the computational study, an apparatus capable of actuating an airfoil with sinusoidal motion was constructed in the NDSU machine shop [24]. The entire unit was mounted to 80/20 aluminum rails rigidly below the wind tunnel such that the whole setup could be moved in any relative direction. The airfoil was fixed to a column such that it can rotate freely along its center axis. The actuation rod behind the center axis was attached to an actuating linear shaft. This shaft moves along a set of linear bearings to keep it on track. A counterweight and connecting arm were machined out of aluminum and arranged in a crankshaft formation in order to produce a sinusoidal action. At the center of the counterweight, a UL 12V DC motor capable of delivering up to 3000 RPM was mounted on a rigid support. The connecting arm is located 15 mm radially away from the center of rotation to produce a maximum stroke of 30 mm. The counterweight was made out of stock aluminum and intended to possess a high moment of inertia in order to maintain stability at high frequencies. To achieve greater dynamic balance, half of the counterweight was machined off on one side to counteract the moment applied by the weight of the rod and any loads induced by the airfoil. The entire fixture

is surmounted to a thick piece of aluminum connected to a platform adjacent to the wall of the wind tunnel.

Figure 2 (a) shows the various assembly parts and their position. At the end of the linear shaft, a rose joint is traveled freely on another shaft indicated as the pitching arm. The pitching arm is connected to the rods inserted into the airfoil and protruded through the acrylic insert. Figure 2 (b) shows the minimum and maximum angle of pitching cycle as read by a Protractor.
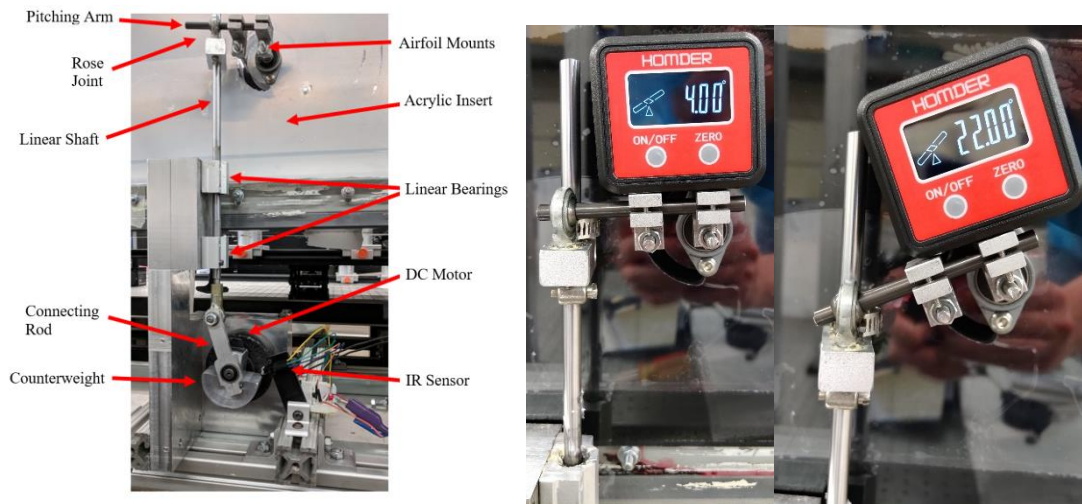
Figure 2. (a) Entire actuator assembly (b) Testing the minimum and maximum angle.

For this experiment, three sweep angles 0^0, 15^0, and 30^0 are used to compare dynamics stall. The airfoils were 3D printed from ABS with two holes running with the pitch angle; one at 25% chord length and another 25 mm behind that. It is important to note that in order to ensure free stream boundary conditions; the span of the airfoil was limited to half of the wind tunnel throat (12 in). This means the maximum span length of the airfoil will be approximately 152 mm or 6 inches. Both holes will be printed about the axis of symmetry. In order to reduce material consumption and mass, a medium infill of 50% will be used for the bulk of the airfoil. Figure 3 (a) below contains a cross section drawing of a test airfoil which was successfully printed with a sweep angle of 30°. Printed airfoils are shown in Figure 3 (b). For testing they were surmounted to a

9

fixed column and allowed to rotate about its aerodynamic center. Inserted into the airfoils, two 3.5 mm rods were used to support the entirety of the airfoil and permanently to the inside of the airfoil with an adhesive. The rods were angled in accordance to the required sweep angle of the airfoil. The rods protrude from the airfoil by 30 mm and are used to surmount the airfoil to the actuating apparatus attached to the wind tunnel. The dimensions of the wind tunnel test section is shown in Figure 3 (c) and Figure 3 (d) shows the actual $\Lambda = 30°$ airfoil mounted in the throat of the wind tunnel.

(a)

(b)

(c)

(d)
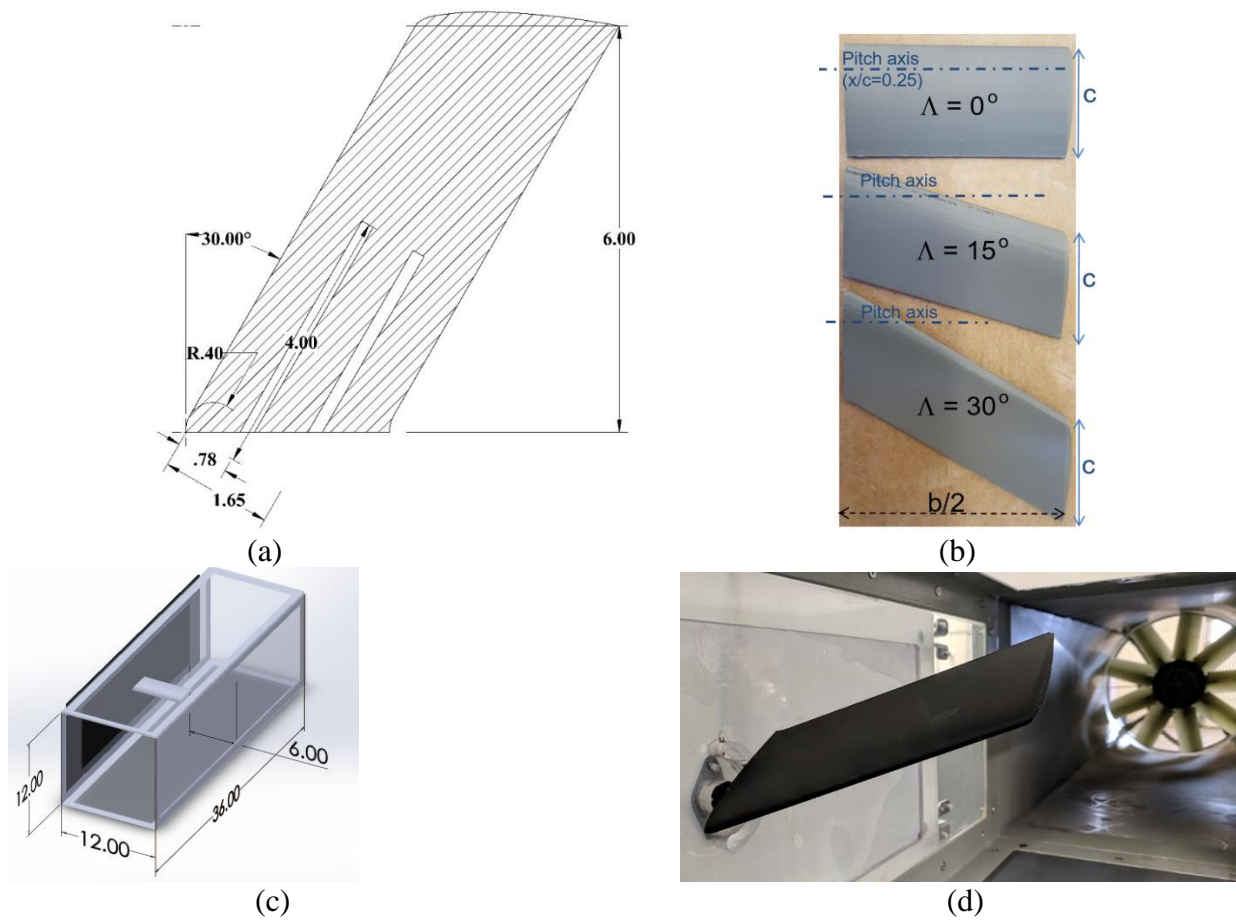
Figure 3. (a) Dimensions and geometry for the NACA0012 airfoil with swept angle $\Lambda = 30°$ (b) 3D printed model of three different sweep wings (c) wind tunnel test section dimensions detail (d) wing mounted in the wind tunnel.

10

Particle Image Velocimetry

In this study, the flow was captured using Particle Image Velocimetry (PIV) [35]. Fundamentally, PIV captures two instances of the flow seeded with particles, one after another, separated by a few microseconds and cross-correlation can be used to determine the displacement of particle ensembles in the flow in small subregions (interrogation cells). Once displacement and time are known for each particle ensemble, velocity of the particle ensemble can be determined. It is intended to capture velocity fields at the surfaces of the wing at several predetermined locations.

It is important to note that since this is an oscillating system, but our point of interest is at a specified angle of attack, the PIV will need to be synchronized ('phase-locked') in order to capture data at the desired phase angle during upstroke and downstroke of pitching cycle. A feedback system was thus incorporated to the actuator in order to consistently capture data at a desired moment of actuation and it is discussed in the subsequent section.

The fundamental setup of the PIV system can be seen in Figure 3. The wing is placed in one side of the wall and there is 6" gap between the wing tip and the other side of the wall. The test section of the wind tunnel is illuminated by a double-pulsed Nd:YAG laser (NewWave MiniLase-III) emitting two laser pulses of 100 mJ at a wavelength of 532 nm with a repetition rate of 15 Hz. The laser beam can then be shaped to a laser sheet (thickness <1 mm) by using a set of mirrors, spherical and cylindrical lenses. The flow, seeded with atomized 'DEHS' oil droplets to achieve particle sizes less than 1μm, is visualized by two La Vision IMAGER LX 2M cameras with a resolution of 1608 x 1208 and interframe capability of 200 ns set up with their axis perpendicular to the laser sheet for image acquisition. For the desired flow speed, the time between images taken was set to $\Delta t = 25\mu s$. The cameras and the Nd:YAG lasers were connected to a

workstation and controlled with ISSI PSG-2 Pulse Generator secondary delay generator which controls the timing of the laser illumination and the image acquisition. LaVision DaVis 10 software [26] was used for control of the parameters of the imaging and controlled by an external trigger.
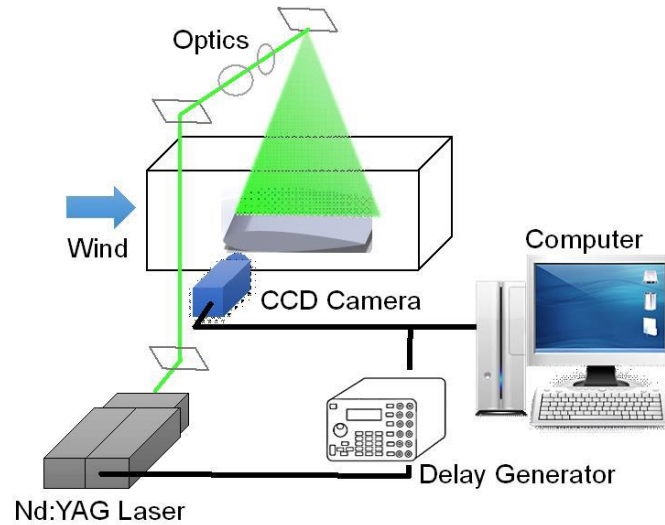
Figure 4. Schematic of standard PIV system.

In this study, with PIV experiment, the data was captured at three planes for three airfoil wings. Our regions of interests are in the mid-plane '50% span', 75% of wing span, and at the wing end-tip (100% span). A thin laser sheet was used for illumination at these regions of interest Figure 5.

(a)   **(b)**   **(c)**
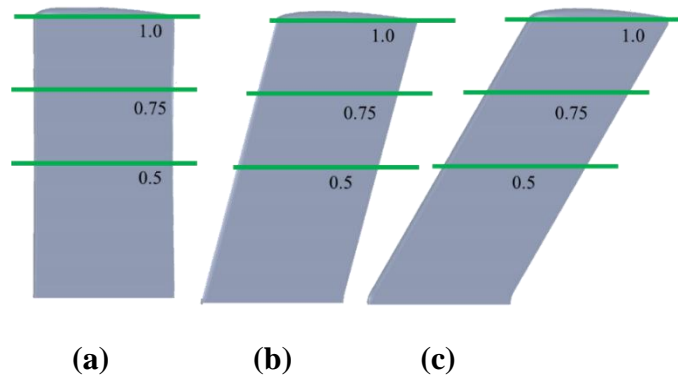
Figure 5. Span-wise locations of 2D PIV data collection (a) unswept (b) 15^0 sweep (c) 30^0 sweep.

Synchronization of PIV and PSP Experimental Setup System

In order to capture data at specific pitching angles ('phases') at any point during the pitching cycle, the following method was created to synchronize the actuator to the lasers and camera. A basic circuit was made using an inferred sensor and a transistor which would be the source of the external trigger. A small piece of tape would pass between the beam of the infrared sensor which would close the gate to a 2222N transistor and create a pulse. This output pulse could be measured easily with an oscilloscope to obtain frequency of rotation. Figure 6 shows the basic function of the rudimentary trigger circuit.

Since the period of rotation is the same for the rotating crank as it is with the pitching cycle, the delay necessary to offset the laser can easily be calculated. The DaVis 10 Software used to capture data with PIV and the external trigger on PTU unit can accept an external signal to trigger the cameras to capture data. Instead of signal generated by PTU unit, an external trigger signal was fed to the PTU generated by output of Infrared sensor during rotation of crankshaft. The output of the external trigger signal is a square wave as shown in the Figure 6 (b). The yellow line in Figure 6 (b) indicates the external trigger signal, and green line indicates the PTU signal output. From, it can be seen that the PTU signal is delayed from the external trigger signal. For PSP experiment, an ISSI PSG-2 delay generator was used to trigger the camera.

<div align="center">

(a)   **(b)**

</div>
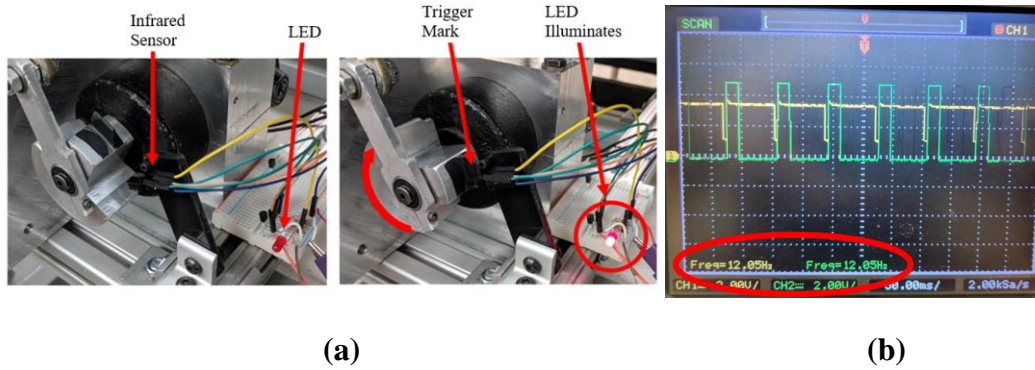
Figure 6. Basic unit of the rudimentary trigger circuit (a) External trigger source (yellow), PTU signal (green) (Oscilloscope screen) (b).

<u>Experimental Setup to Measure Robustness of the Structure</u>

In this study, the pitching airfoil was designed to be capable of generating a sinusoidal pitching motion at various frequencies such as 15 Hz and 30 Hz to achieve reduced frequencies of interest k = 0.1 and 0.2. Usually, this requires a robust structure to prevent vibrations that could influence the flow structures and even damage the airfoil and its holding structure. To measure the robustness of the design, a simple experiment was performed. In this experiment, a camera was placed on top of the wind tunnel with a Laser illuminating the suction side of the airfoil, as shown in Figure 7. The surface of the airfoil was marked with black dots (Figure 7). Similar to the phase-locked data acquisition in the PIV section, a single frame image was captured at a specific phase angle during the pitching cycle. The captured data will show the position of the black marker at a particular phase angle during the cycle-to-cycle pitching motion. The captured raw images are shown in Figure 8. From observing the data, we can see that the markers remain in a similar position for a specific angle (in this case, the angle was chosen to be 110 downstroke). This proves that the effect of vibration is very negligible during the pitching motion of the airfoil. For more quantification, an X and Y correlation was performed to show the displacement of the pixel of the airfoil surface during the pitching motion. From 80 instantaneous cases, the average vector length is shown in Figure 9. The results show that the average vector length obtained from the correlation

14

of the airfoil surface during the pitching cycle is very close to zero. This further proves that the structure has high robustness during the pitching and vibration has a negligible effect on the flow structure. Similarly, the correlation vector was also computed for sweep 150 and 300 airfoils at 190 downstroke. The results, as shown in Figure 9 (b, c), indicate similar characteristics.
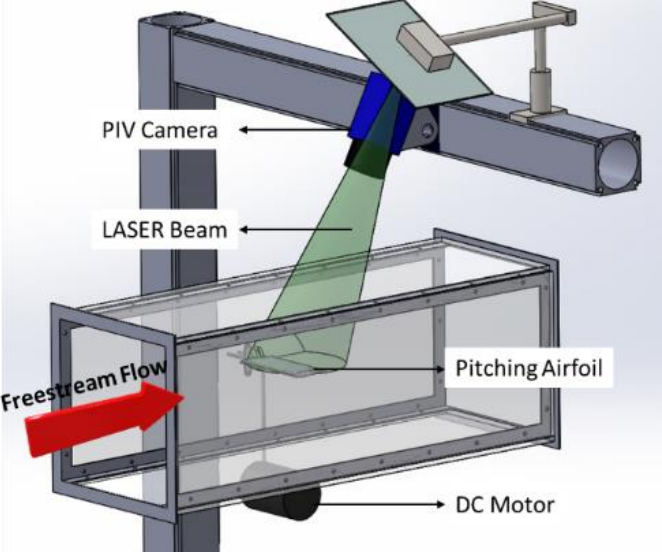
Figure 7. Experimental setup of measuring the robustness of the structure.
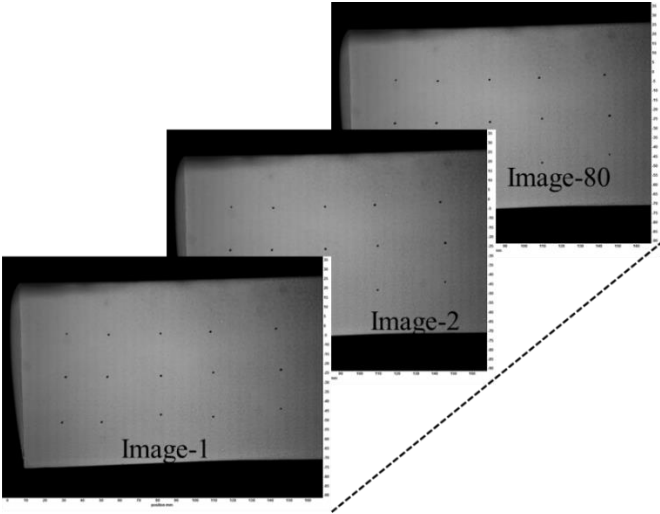
Figure 8. Raw image captured during pitching cycle at 11^0 downstroke.
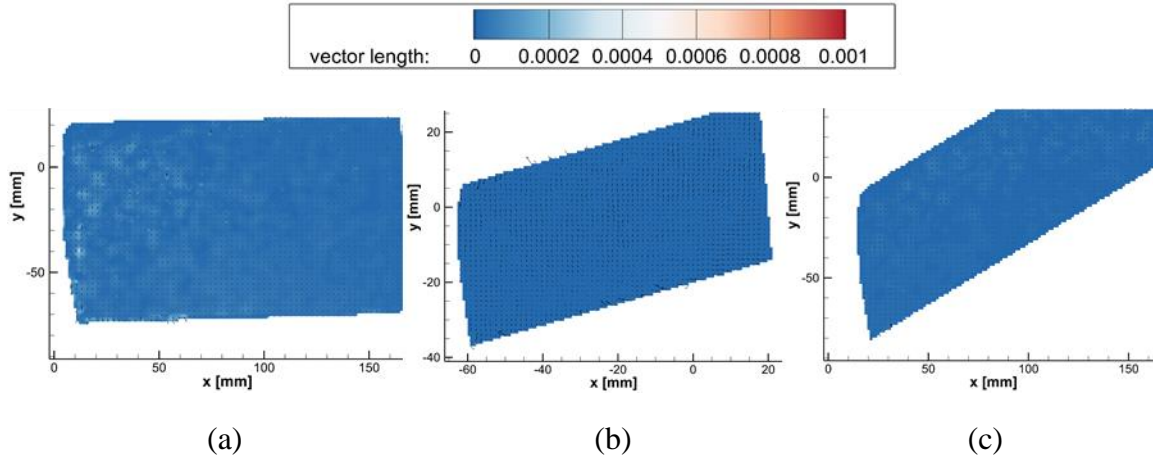
Figure 9. Average vector length calculated from the instantaneous correlation for (a) unswept at 11^0 downstroke (b) sweep 15^0 at 19^0 downstroke, and (c) sweep 30^0 at 19^0 downstroke.

Results and Discussion

In this section, PIV results and analyses are presented and discussed. All the instantaneous and average velocity maps are shown for individual sweep wings at various phase angles and three planes. During the different flow characterizations from the data, the following observations should be considered. Firstly, as noted in the setup section, the phase-locking synchronization of the pitching mechanism was robust and gave only minor (<1%) electronic and mechanical/vibrational jitter in the phase location (and AoA). The flow visualization indicates that the variation of angle due to wind load is negligible. The PIV data was captured for two phases of the pitching cycle: an upstroke (↑) and a downstroke (↓). When the leading edge (LE) goes up and the trailing edge (TE) goes down is called upstroke (↑) or pitch up. The reverse direction of motion of LE and TE is called downstroke (↓) pitch down. The schematic of the upstroke and downstroke phases is shown in Figure 10.
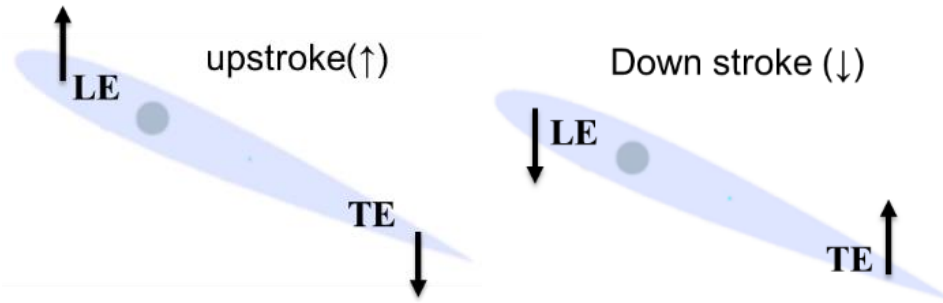
Figure 10. Schematic of upstroke and downstroke during pitching cycle.

Flow Structure over Pitching Unswept Wing, $\Lambda = 0^0$

Flow structure at 19^0 downstroke ($\downarrow$)

In the PIV campaign, the data was collected for unswept airfoil wing at every two degree (11^0 to 19^0) interval during pitching cycle and also at minimum and maximum position of pitching motion ($4^0 - 22^0$ AoA). From the observation of 100 instantaneous cases, it is found that the pitching down/downstroke ($\downarrow$) phases are comparatively more unsteady in nature in contrast to pitching up/upstroke ($\uparrow$) cases. The flow is phase-locked for upstroke ($\uparrow$) phase angles until the airfoil stalls at high incidence angle. To illustrate the unsteady nature of flow during downstroke phase ($\downarrow$) two samples with qualitative flow visualizations and their instantaneous PIV maps (using 'PIVlab' software [27]) at three spans are shown in Figure 11 ('Sample 1' and 'Sample 2') followed by the phase-averages and standard deviations in Figure 12. From the two samples, randomly selected from the set of 100 images taken at the phase, and the average quantities, important flow features can be inferred.

The set of the data in Figure 11 is comprised of characteristic three-dimensional (3D) vortical structures that at mid (50%) span have a 'larger' scale (with integral size on the order of half-wing chord) and 'high' unsteadiness (compared to that in the other spans), that at 75% span have a 'medium' scale (with integral size on the order of a fraction of half-wing chord) and

17

'medium' unsteadiness, and that at the wing end-tip (100%) span flow remains attached until mid-chord where turbulent secondary separation with 'smaller' scales and 'unsteadiness' appear and TE vortex structures form as a tip vortex (TV). The flow pattern characterized by a larger structure in the mid span that is approximately halved in size in the 75% span and that has completely disappeared in the wing tip region (due to a finite length wing boundary condition at the end-tip) is indicating the existence of vortical three-dimensional (3D) structures having, at this phase, approximately half-chord integral size; this vortex inferred from the 2D slices has thus consistent similarities with the various evolving vortex structures in the simulations [1] generated during the pitch down maneuver. The flow 'phase-locking' exhibits three different levels in each of the three spans with lower repeatability in the mid span and increasing repeatability towards the end tip; this repeatability is di-similar to that expected from the simulations that established repeatability at every cycle. During the experiment, it is observed that, near the 50% (mid) span, more unsteadiness and disorderly (or chaotic) patterns happen from cycle to cycle thereby loosening some of the repeatability that simulations capture. The amount of in-phase unsteadiness in the experiment can be tied to the wind tunnel boundary and free-stream conditions, end-tip non-infinite boundary, and the fact that free-stream conditions are not absolutely uniform and symmetric in all sides. In addition, some natural chaotic flow pattern from different phase instances cannot be ruled out. Although these conditions were designed to provide as symmetric and infinite boundary conditions as possible some factors during pitching, such as the amount of blockage, can have variable implications. Quantification of flow repeatability will be further assessed through calculation of phase-coherence and phase-randomness during the phase-average studies in the next sections.

In addition to these observations, it can be noted that, in one instance of the mid wing span (Figure 11. a1-d1) vortex is large (some vectors in the vortex motion frame of reference are also

18

shown superposed to the visualization of Figure 11. a) while in the other instance shown (Figure 11. a2-d2) a vortex is not immediately identifiable but instead is part of a vertical burst stream that is just preceded by a vertical downwash of flow-reattachment stream occurring after the first separation region (LEV region). These differences between instances are still within the general expectations of a large separated flow and a DSV formation. They become much less pronounced in the 75% span (Figure 11. b-e's) and almost inappreciable in the wing tip (Figure 11. c-f) where flow shows both, the secondary separation region and the tip vortex (shown in detail with vorticity in the sample in Figure 11. f1) surrounded by the free-stream. These vortex appearances in the three spans is consistent with the existence of a finite span vortex structure in the middle of the wing span such as those reported in the simulations [1] as 'arch-ring' depending on the pitch phase.
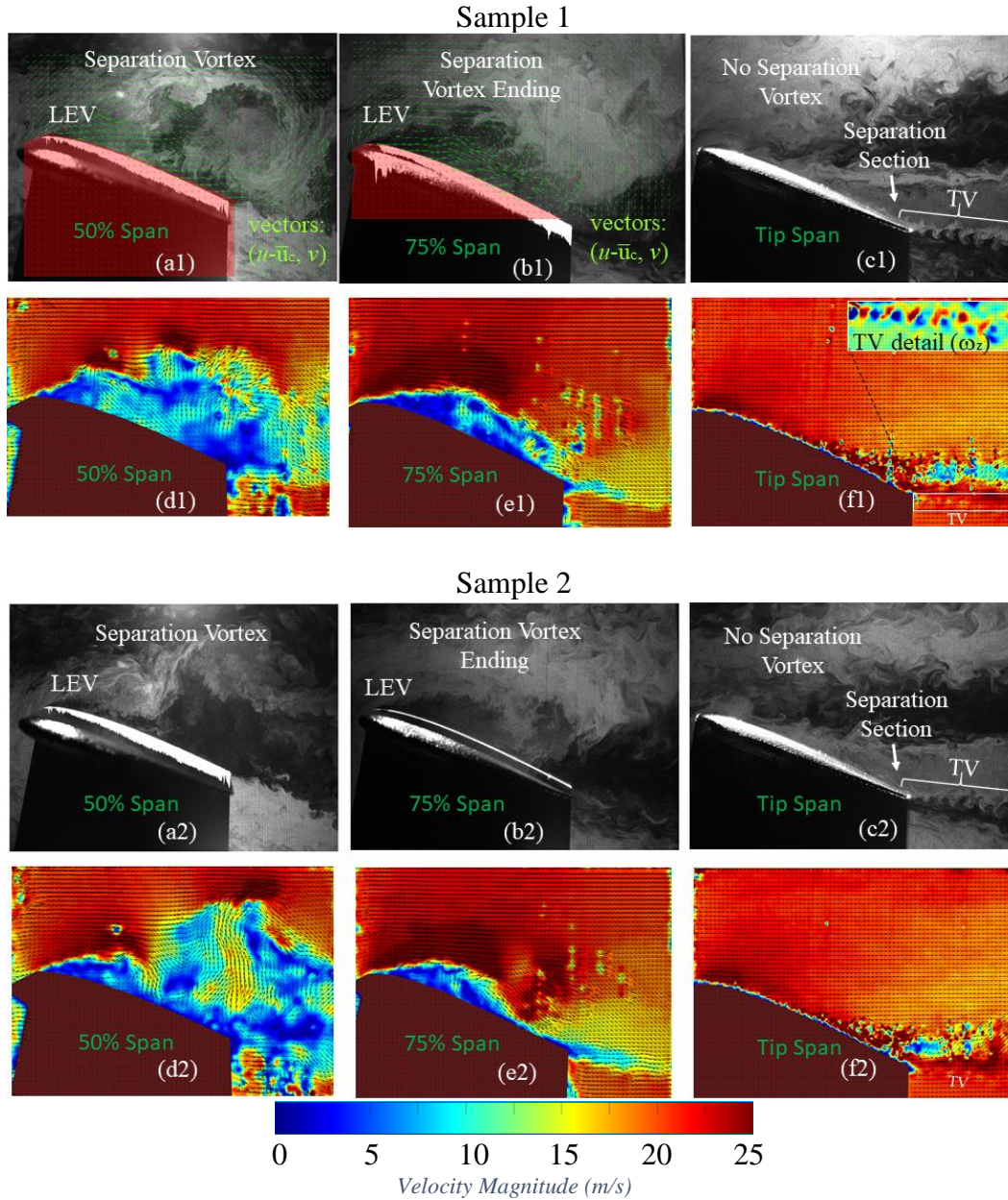
Sample 1

Sample 2

Figure 11. Two samples (1, 2) of spanwise instantaneous flow-visualization (a-c) and PIV (d-f) for the unswept wing at the 19o pitching-down phase at 50% (mid-wing) (a, d), 75% (b, e), and 100% (wing tip) spans (c, f). Flow regions, Leading-Edge Vortex (LEV) and Tip Vortex (TV) are indicated. Some vectors on flow visualization are drawn (a1, b1) to indicate vortex-reference motion and a detail of the (swirling) TV spanwise vorticity (ωz) is shown in 'f1' at Re=1x105, k=0.2.

Phase average and standard deviation at 19^0 downstroke ($\downarrow$)

Figure 12 shows the average and the standard deviation for the set, which was calculated at 19^0 downstroke ($\downarrow$) phase angle from 100 instantaneous velocity instances. The results show that a large recirculation region exists at 50% wingspan, as shown in Figure 12 (a1). The average integral size of recirculation region decreases significantly at 75% wingspan and the recirculation region vanishes at the wing tip (Figure 12-b1 and c1). Due to the existence of flow randomness at mid-span, high standard deviation exists in the shear layer of airfoil. At 75% and wing tip, the intensity of the turbulence reduces compare to 50% wingspan, as shown in the Figure 12 (a2-c2).
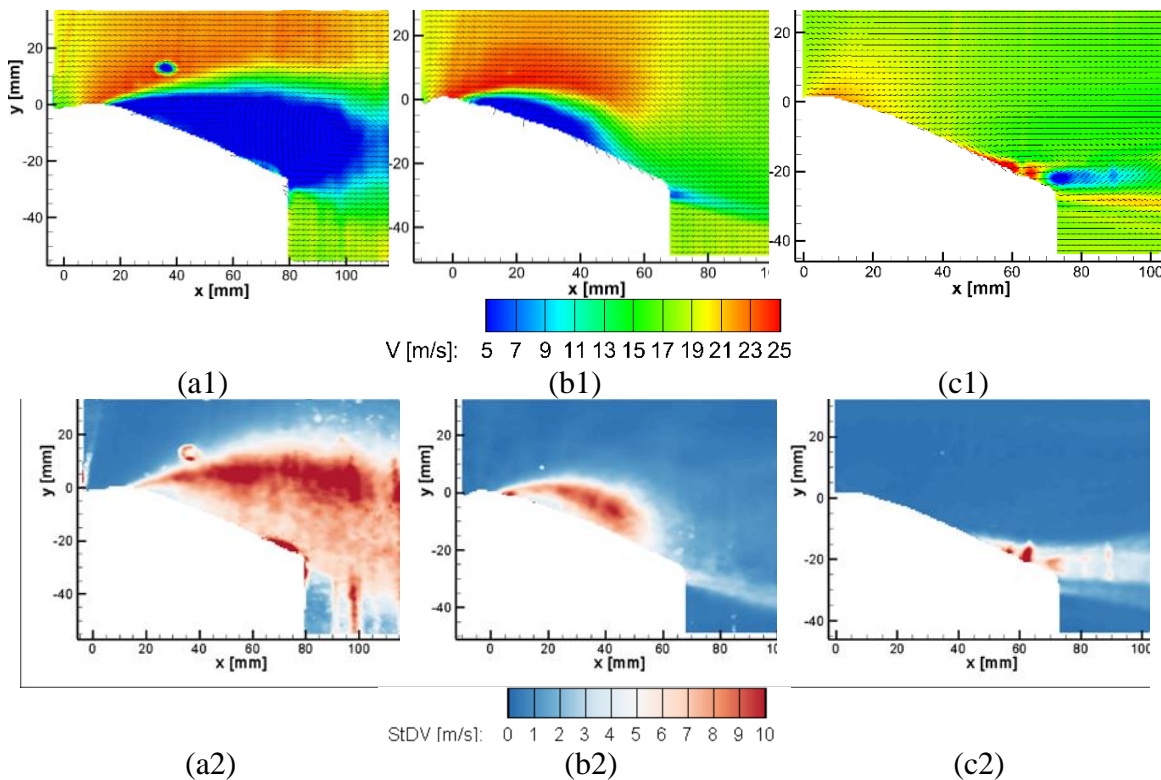
Figure 12. Average PIV velocity (top) and standard deviation (bottom) maps from the unswept wing 19° pitching-down phase case at 50% (midspan) (a), 75% (b), and 100% (wing-tip) (c) spanwise planes. Re=1x10^5, k=0.2.

POD analysis to determine phase coherence

While the average, standard deviation, and visualization of individual instantaneous instances establish the pattern repeatability in several flow regions, a more assertive measurement of phase-coherence is proposed using proper orthogonal decomposition techniques (POD) [28-34]. The details of the POD are provided in the Appendix section. The POD is used to extract the dominant modes from flow features. In this analysis, the POD was applied to the phase angle of 19^0 downstrokes ($\downarrow$) at three spans of the airfoil wing, shown in Figure 13. From the 100 instantaneous velocity field, the dominant modes were extracted. The results indicate that more number of dominant modes contain coherent dominant structures at 50% wingspan.

On the other hand, for 75% and the end tip of the airfoil, the energy of dominant flow structures quickly dissipates. In other words, it can be said that in order to reconstruct the original velocity contour, it will take more modes for 50% wingspan compare to at 75% and 100% (wing tip) wingspan due to the high unsteady and randomness of the flow for downstroke phase angles. This observation from POD is crucial because of twofold reasons. Firstly, it will describe the repeatability and organization of the experimental flow field in the wind tunnel conditions. Secondly, it will determine how to establish a sound framework for comparisons with the numerical simulations [1] that produce/assume a perfectly phase-locked flow pattern, in fact, simulating a single cycle.
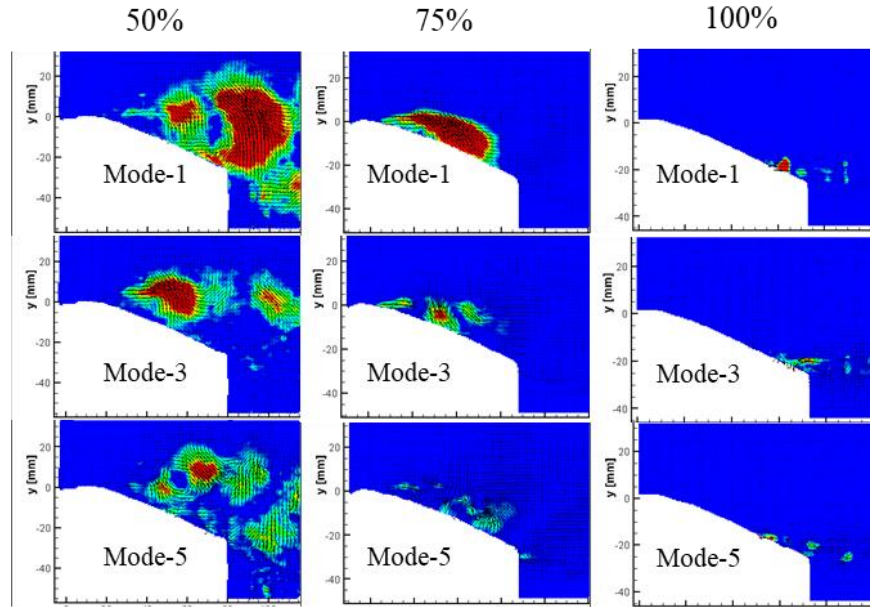
Figure 13. POD modes for unswept wing at 19º pitching down. The 75% span and end-tip mode energy quickly dissipate after first few modes (indicating phase-coherence) while the 50% mid span, housing the large unsteady vortex, requires more modes to fully reconstruct (indicating more phase randomness). Re=1x10⁵, k=0.2.

Change of Flow Structure at Various Phase Angles during Downstroke (↓) and Upstroke (↑)

of Pitching Cycle

Now, the variation of the flow structures with the change of phase angle during the pitching cycle is provided. The phase angles during the pitching cycle are divided into an upstroke (↑) and a downstroke (↓). As mentioned earlier, the flow structure varies significantly for upstroke and downstroke of pitching cycle. During the pitching cycle of airfoil, it starts from 22^0 and then travel to 4^0 during the downstroke and then it travels back from 4^0 to 22^0 during the upstroke. The velocities contours that are shown here are non-dimensionalized with respect to freestream velocity U.

The instantaneous and average velocity contours of downstroke phase angles, including minimum and maximum phase angle, are shown in Figure 14 and Figure 15, respectively. When the airfoil starts pitching from 22^0, the separation burst occurs at mid-span, at 75% wingspan a

23

small recirculation region forms, and at 100% wingspan no separation region is observed. However, a strong trailing edge wake can be noticed in the flow field. As the airfoil continues further with downstroke motion, the separation burst starts to grow more at mid-span due to the upward motion of the trailing edge of the airfoil. As the angle reaches 15^0, 13^0, and 11^0 during downstroke motion, as shown in Figure 14 (d-f), the flow starts to attach at the leading edge (LE), and the separation burst shift toward the trailing edge of the airfoil. At 75% wind span at 15^0, 13^0, and 11^0 downstroke phases, a small separation burst is observed at the very end of TE, whereas the flow pattern remains similar at the wing tip for those phase angles. As the airfoil reaches 4^0, the flow becomes completely attached at all three spans of the airfoil

The average velocity calculated from 100 samples at the similar phase angles during downstroke motion are shown in Figure 15. The findings in the average velocity maps show that at a high angle during the downstroke of pitching, the flow separation is pronounced at every cycle. The only difference with instantaneous and average velocity contour is that on instantaneous velocity contour, the downstroke motion creates small secondary vortical flow in the boundary of the separated region and freestream flow, which varies from cycle-to-cycle. As a result, the averaging of all 100 instant cases at a specific phase angle smooths those secondary vortical flows in the boundary. The calculated average provides useful information about the phase coherence of the flow from cycle to cycle. At 100% wingspan during the downstroke, the flow remains phase-locked. This phenomenon can be observed by comparing the instantaneous and calculated average velocity map.

The instantaneous and average velocity contour of the upstroke motion of the pitching cycle is shown in Figure 16 and Figure 17. The results in instantaneous and average velocity contour show that the flow remains phase-locked and attached during its upstroke maneuver for

all of its phase angles except 17^0 and 19^0. At 17^0 upstroke angle, a small recirculation region forms in the leading edge, and the flow re-attaches at the trailing edge of the airfoil surface. This small region corresponds with the laminar separation bubble (LSB) [1-13]. This small recirculation region (LSB) forms at the specific phase angle during every pitching cycle. Because of the existence of LSB in every pitching cycle, the average velocity contour shows the LSB formation in the LE at 17^0 upstroke angle, presented in Figure 17 (d). As the angle reaches 19^0, the separation bubble on the airfoil surface grows in size. This can be observed in Figure 16 and Figure 17 (e).

The difference of flow structure for upstroke and downstroke maneuver of pitching cycle relates to the motion of the wing. When the leading edge (LE) goes up and the trailing edge (TE) goes down during upstroke, it creates a shear layer roll in the LE. With the increased angle during the upstroke, this shear layer roll creates a slight separation and a reattachment of flow in the TE. As the angle of attack during the upstroke of the pitching cycle increases, the shear layer roll of the flow grows, and a more prominent recirculation region appears. When the airfoil starts pitching from a high incidence angle during the downstroke, the upward motion of TE in addition to the negative pressure that builds upon the suction side of the airfoil surface contributes to high unsteady and non-repeatable flow.
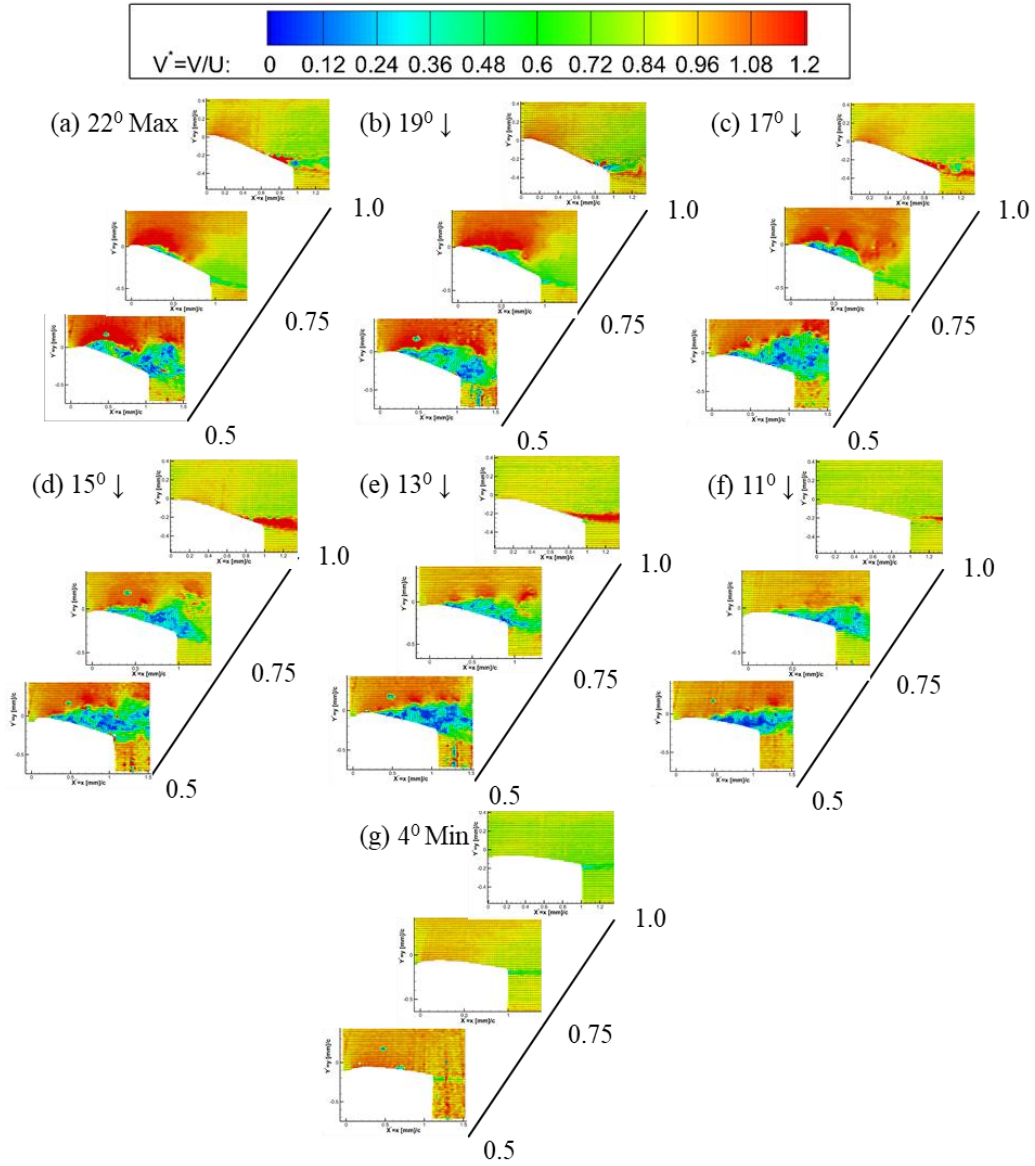
Figure 14. Instantaneous velocity contour of downstroke phase angles for unswept airfoil when Re=1x10^5 and reduced frequency, k=0.2.

26
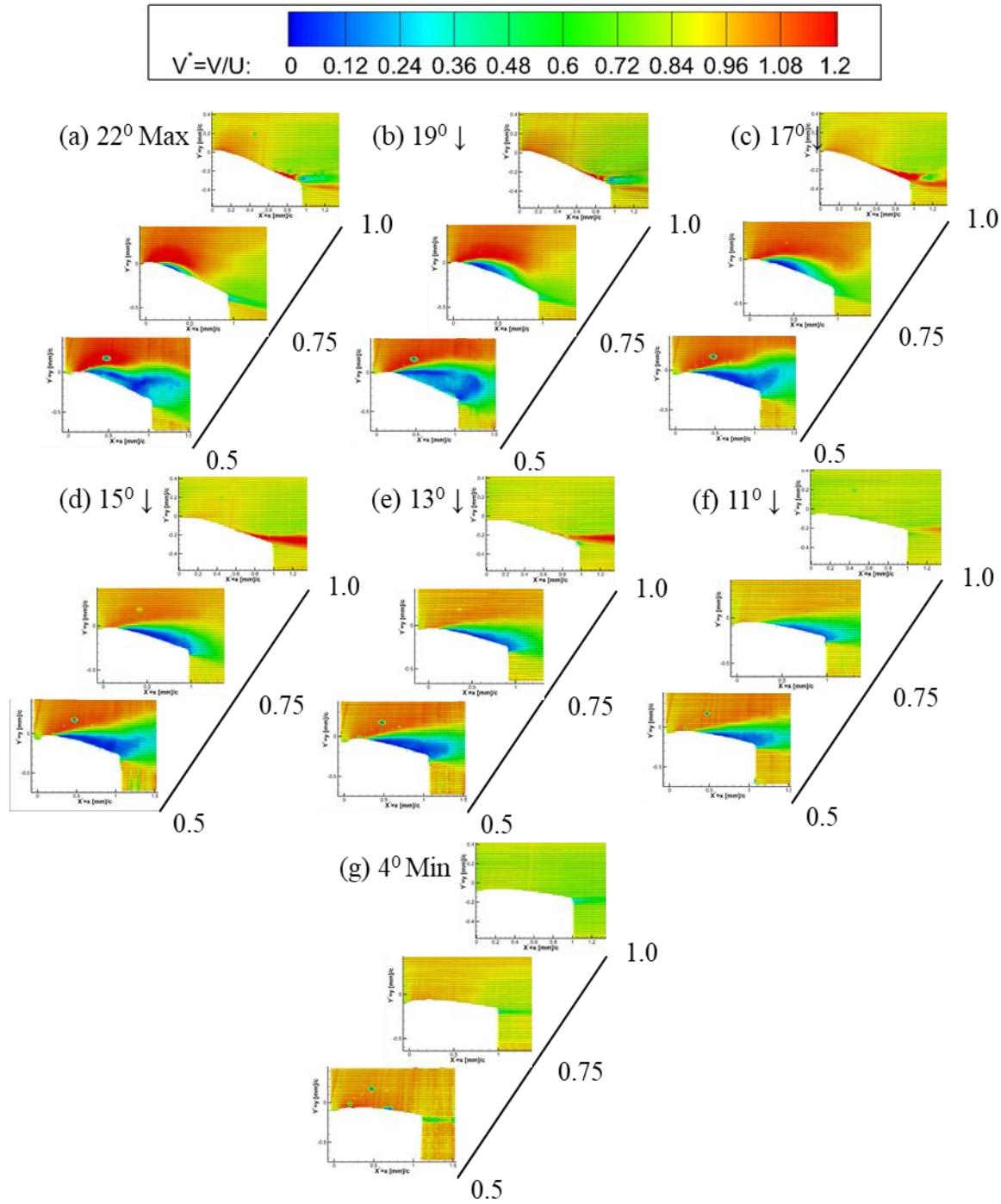
Figure 15. Average velocity contour of downstroke phase angles for unswept airfoil when Re=1x10^5 and reduced frequency, k=0.2.
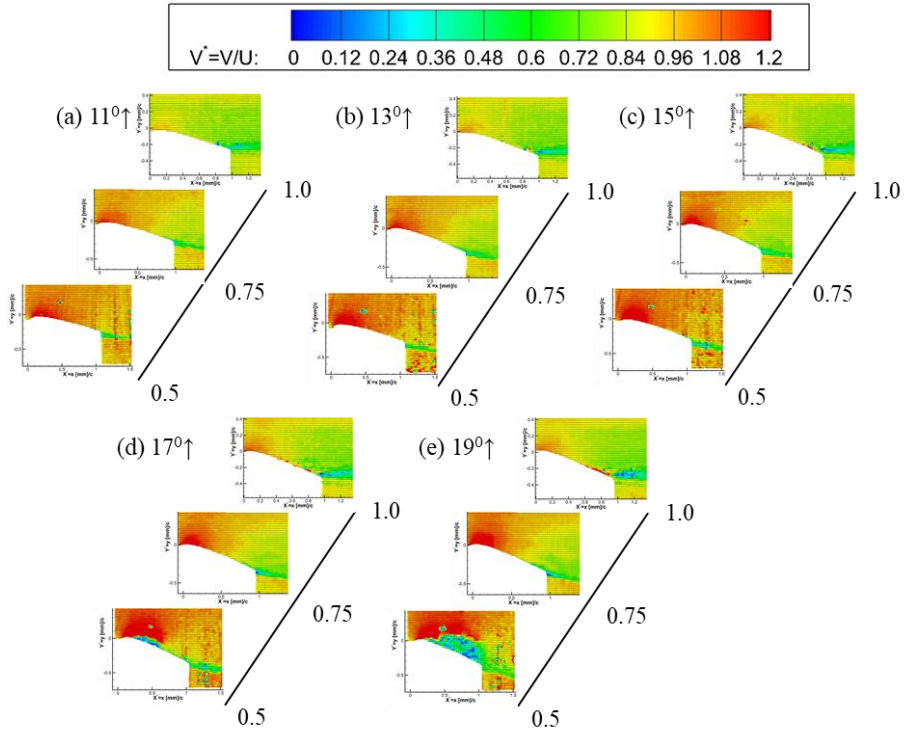
Figure 16. Instantaneous velocity contour of upstroke phase angles for unswept airfoil when Re=1x10^5 and reduced frequency, k=0.2.
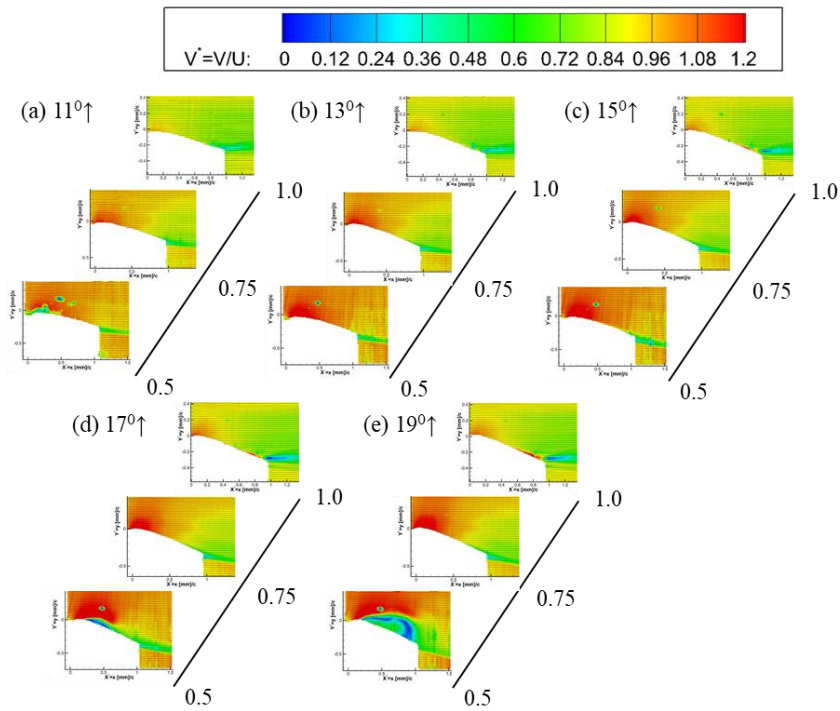
Figure 17. Average velocity contour of upstroke phase angles for unswept airfoil when Re=1x10^5 and reduced frequency, k=0.2.

28

Effect of Increased Sweep Angle, Λ =15^0 and 30^0

In this section, the flow structure of sweep 15^0 and 30^0 airfoil is discussed based on the phase average of velocity calculated from 100 instantaneous velocities taken at a specific phase angle during the pitching motion of the airfoil. During the downstroke maneuver, the phase angles are arranged from 22^0 max to 11^0, and during the upstroke maneuver, the phase angles are arranged from 11^0 to 19^0 at an interval of every two-degree phase angle.

When the downstroke motion continues starting from 22^0, the flow remains completely separated. A more prominent recirculation region grows more in the 75% wingspan region than 50% and 100% wingspan. As the downstroke motion continues, at 19^0 and 17^0, the separation burst with recirculation region forms consistently in each cycle. During the downstroke maneuver, unlike unswept airfoil, the wing tip has unsteady flow separation. This happens due to the change of shape and boundary condition from the unswept airfoil. As the downstroke motion continues and the phase angle drops to a lower angle, the recirculation region due to separation burst decreases. At 100% wingspan, the flow starts to attach at 11^0. The observation indicates that the downstroke motion of the pitching airfoil produces 3D vortical structures, and the three-dimensionality of flow becomes more pronounced close to the 75% wingspan.

On the other hand, during the upstroke maneuver, the flow remains attached until flow separates at a high phase angle, which can be observed in Figure 19. The results show that the flow remains attached at 11^0 and 13^0 phase angles during upstroke motion. As the phase angle reaches 15^0, a small recirculation region forms at 75% wingspan. This small recirculation region forms at the leading edge (LE) and is reattached to the trailing edge forming the laminar separation bubble (LSB). As the phase angle increases to 17^0, this separation bubble grows larger at 75%, with a small LSB at 50% and 100% wingspan. As the upstroke motion continues and the phase angle

becomes 19^0, the flow is completely separated, and an aerodynamic stall happens. At this condition, the recirculation region grows from 50% to 75% wingspan and reduces towards 100% wingspan.

With the increase of sweep angle of the airfoil to 30^0, the flow structure significantly changes. The average velocity contour for sweep 30^0 is shown in Figure 20 and Figure 21. The results show that with the increased sweep to 30^0 and during the downstroke motion of the airfoil, the separation of the flow shifts further towards the wing tip. At 50% wingspan, the flow remains attached for all the phase angles. Small recirculation region forms at 75% and 100% wingspan until the phase angle reduces to 11^0 during downstroke maneuver.

For the upstroke maneuver, the flow remains attached from 11^0 to 17^0. At 19^0 phase angle, a small recirculation region appears in the middle of the airfoil. The results are shown in Figure 20, and Figure 21 prove that increasing airfoil sweep angle to 30^0 delays the stall during the pitching within the range of 4^0 to 22^0.

The results obtained from the airfoil with a sweep angle of 15^0 and 30^0 give an important insight into the flow structure and its relation with the sweep angle of an airfoil. For pitching unswept airfoil, the existence of the 3D vortical structure is pronounced in the area close to the 50% wingspan. As we move to 75% wingspan, the vortical flow starts to decrease. This indicates that the vortex structure associated with pitching unswept airfoil forms in the center of the airfoil. As the sweep angle increases to 15^0, the vortical structures shift further towards 75% of the wingspan, which moves towards the wing tip when the sweep angle changes to 30^0. The finding in this section is very similar to the computational study [1]. Their results show that the arch-shaped vortex during the pitching cycle forms at the center, with the change of sweep angle to 15^0 and 30^0 shifts the position of these arch vortex towards the wing tip. In this 2D PIV study, the data

30

obtained in the three planes is sectionally consistent with the 3-dimensionality like that of an arch vortex. Although the shape of the actual vortical flow needs to be verified further with tomographic PIV, the change of the position of the 2D vortical flow with sweep angle agrees with the study [1].
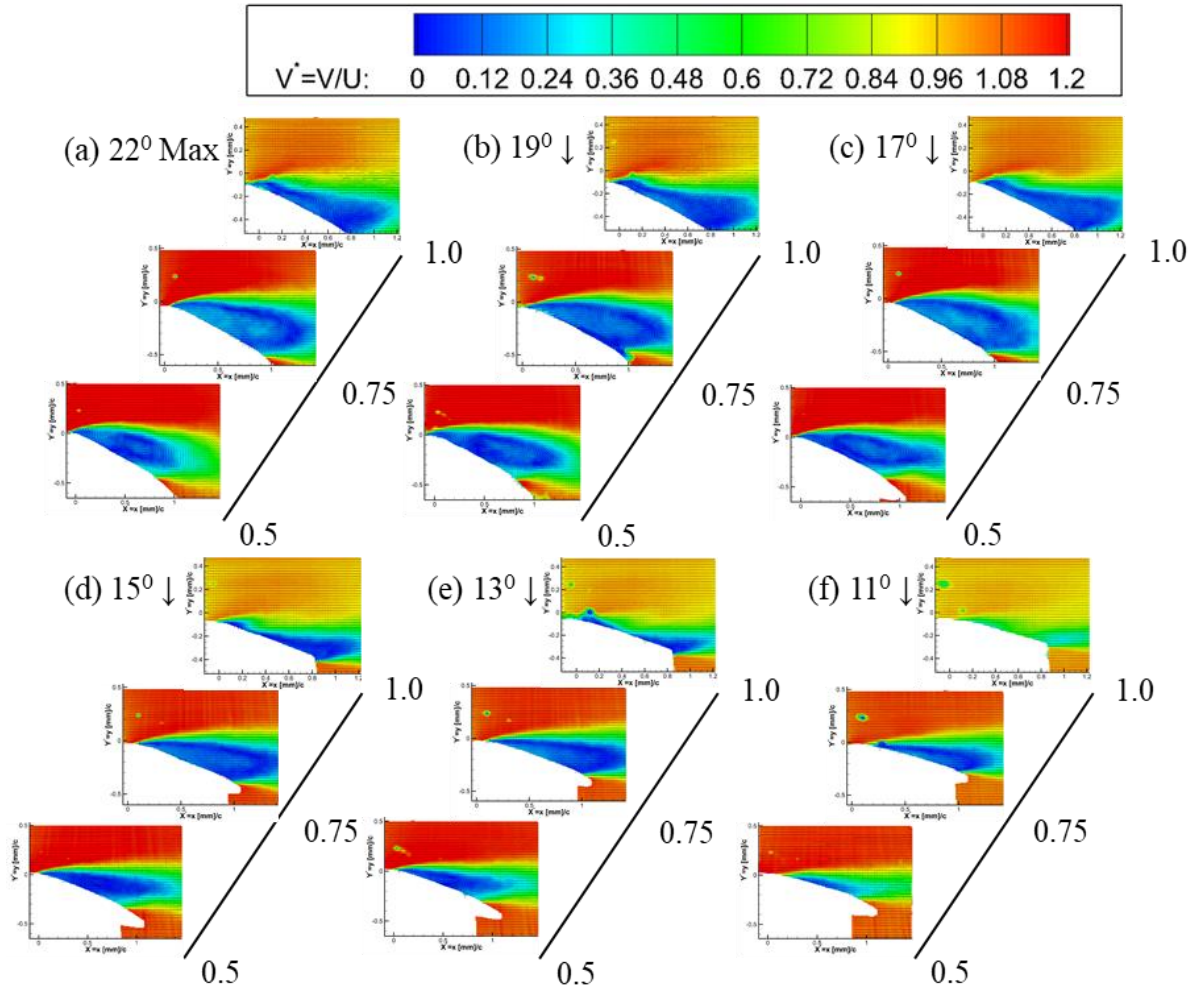
Figure 18. Average velocity contour of downstroke phase angles for sweep 15^0 airfoil when $Re=1x10^5$ and reduced frequency, k=0.2.

Figure 19. Average velocity contour of upstroke phase angles for sweep 15^0 airfoil when $Re=1x10^5$ and reduced frequency, k=0.2.

Figure 20. Average velocity contour of downstroke phase angles for sweep 30^0 airfoil when $Re=1x10^5$ and reduced frequency, k=0.2.

Figure 21. Average velocity contour of downstroke phase angles for sweep 15^0 airfoil when $Re=1\times10^5$ and reduced frequency, k=0.2.

Effect of Change of Relative Frequency with Respect to Freestream Velocity

In this section, the effect of relative frequency with respect to freestream velocity is discussed. Two representative phase angles during the downstroke and upstroke phase are shown in Figure 22 and Figure 23 for the unswept airfoil. The average velocity is non-dimensionalized with respect to the freestream velocity and shown with the same range of velocity contour to understand the effect of increased Re number. During the downstroke motion of the pitching cycle, Figure 18 shows that at 50% wingspan, the recirculation region becomes narrower and grows more toward downstream. At 75% wingspan, the integral size of the separation increases in twice for $Re=2x10^5$ and k=0.1 compared to $Re=1x10^5$ and k=0.2. At 100% wingspan, the strong TE wake is absent for a higher Re number.

The upstroke phase during the pitching cycle, cases at 17^0 and 19^0, is shown in Figure 23. The results clearly show that due to increased Re number, the flow separation propagates more at $Re=2x10^5$ and k=0.1 at those specific angles than $Re=1x10^5$ and k=0.2. As k decreases, the flow tends to separate more like a static airfoil with NACA 0012 airfoil section. This also indicates that higher reduced frequency delays the aerodynamic stall; even higher reduced frequency creates a complex unsteady 3D vortical flow during its pitching cycle.

One representative case is provided in Figure 24 for the sweep 15^0 airfoil,.A similar trend with more significant flow separation due to increased Re number is observed. However, for a higher sweep angle of the airfoil, the flow remains mostly attached and delays the stall even for increased Re number.

35
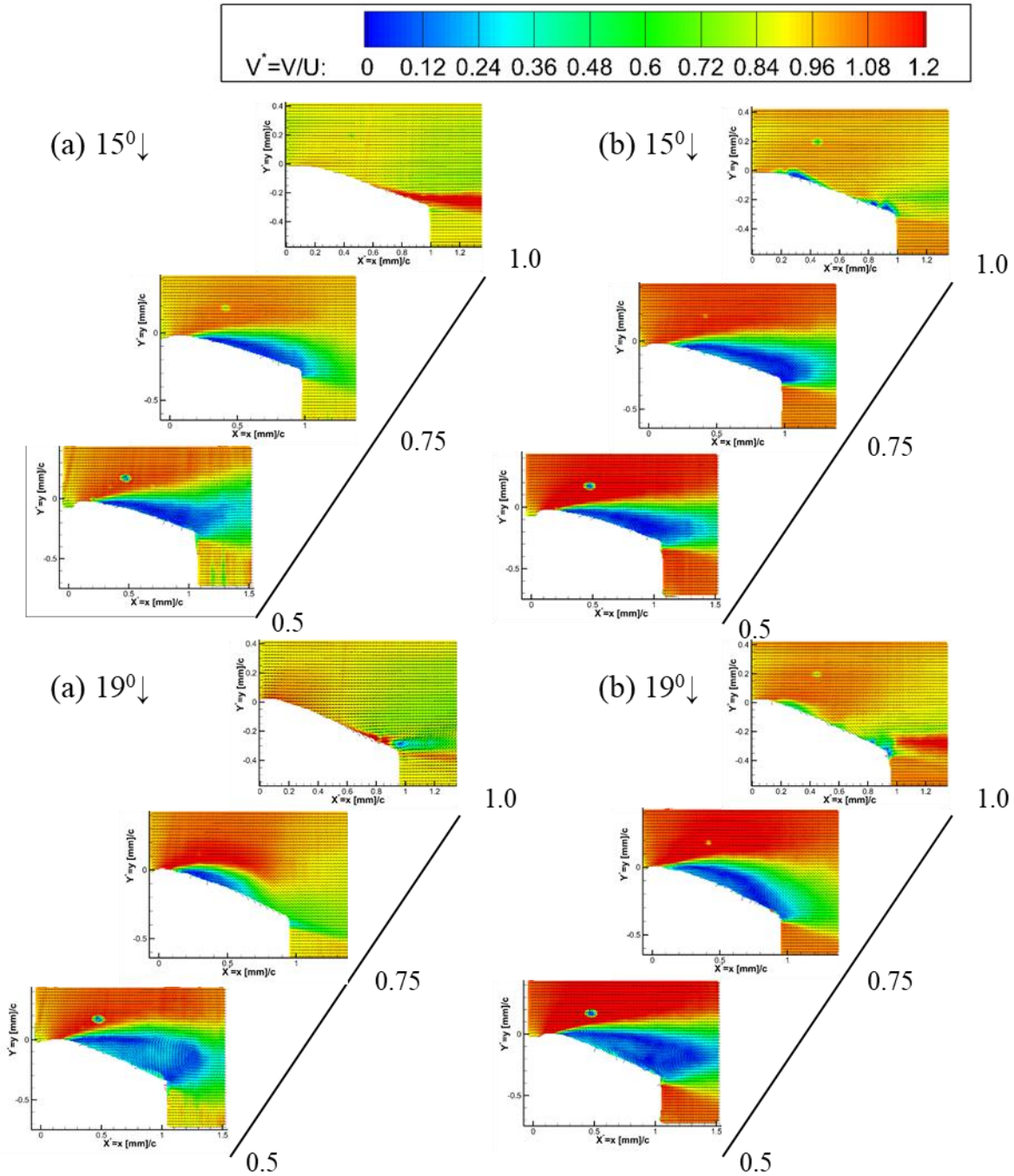
Figure 22. Average velocity contour for unswept airfoil when the (a) Re=1x10^5 and k=0.2 (left column) and (b) Re=2x10^5 and k=0.1 (right column) during downstroke phase of pitching cycle.
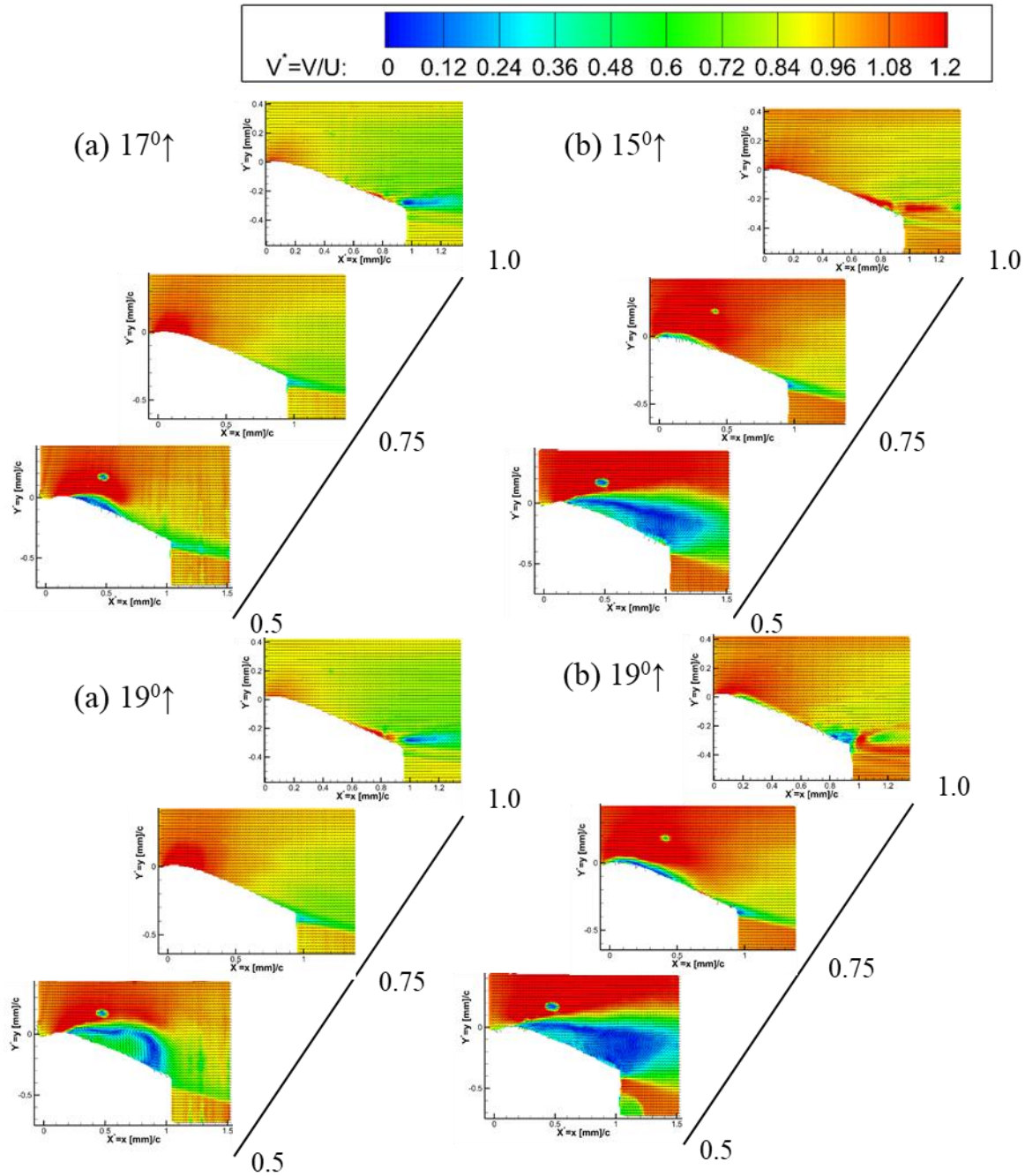
Figure 23. Average velocity contour for unswept wing when the (a) Re=1x10^5 and k=0.2 (left column) and (b) Re=2x10^5 and k=0.1 (right column) during upstroke phase of pitching cycle.

37
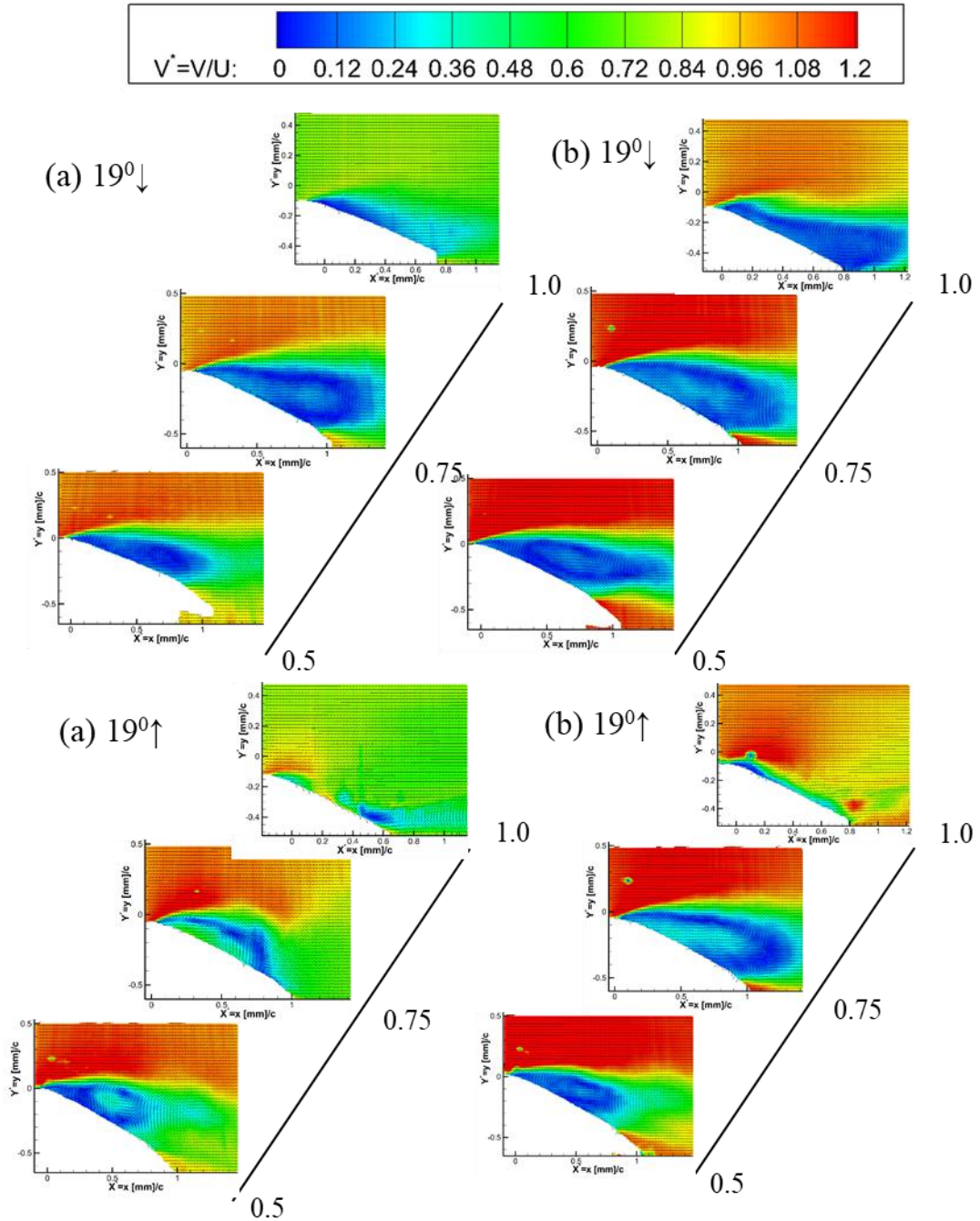
Figure 24. Average velocity contour for sweep 15^0 at 19^0 phase angle during downstroke (top row) and upstroke (second row) of pitching cycle when (a) Re=1x10^5 and k=0.2 (left column) and (b) Re=2x10^5 and k=0.1 (right column).

38
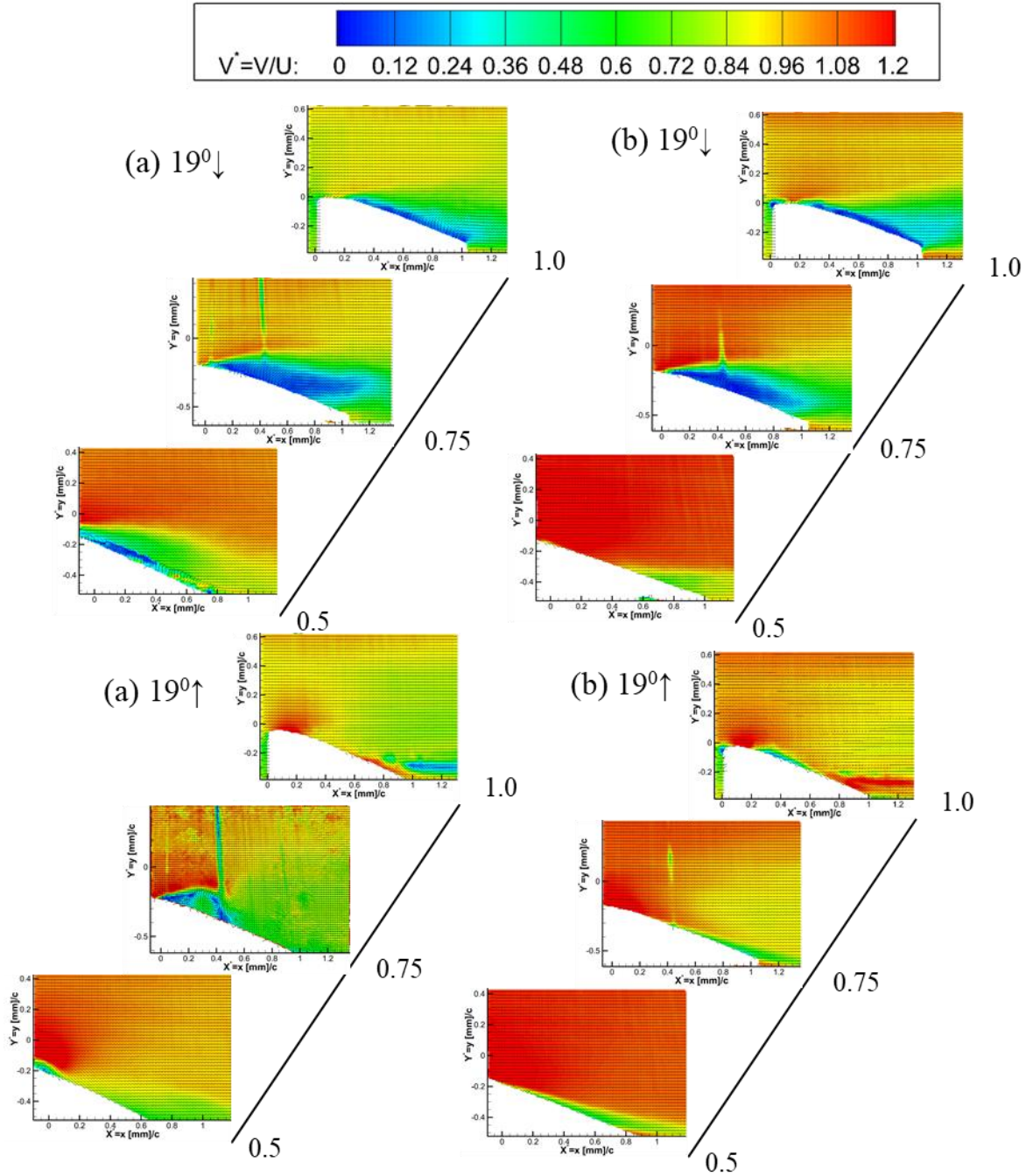
Figure 25. Average velocity contour for sweep 30^0 at 19^0 phase angle during downstroke (top row) and upstroke (second row) of pitching cycle when (a) Re=1x10^5 and k=0.2 (left column) and (b) Re=2x10^5 and k=0.1 (right column).

Chapter Summary and Conclusion

   A 2D PIV study has been conducted to see how the flow characteristics change with the change of sweep angle of a finite aspect-ratio wing as reported in numerical simulations [1]. The experiment was conducted for two different flow conditions. The flow conditions are Re=1x10^5 and reduced frequency, k=0.2, and Re=2x10^5 and reduced frequency, k=0.2. The sweep angles of the airfoil were chosen Λ= 0^0, 15^0, and 30^0 to match those of the numerical simulations [1]. The data was taken at three span-wise locations, 50%, 75%, and 100%. The range of pitching is from 4^0 to 22^0. During the pitching motion, the data was taken during downstroke and upstroke phases at three different span-wise locations.The following summarizes the experiment and observations:

- A 2D PIV experimental study was performed to show flow structures during pitching motion of a finite-aspect ratio wing with three swept angles.

- The results indicate that when the wing is pitching motion, the downstroke phase angles are more unsteady. The flow has less repeatability and coherence. The observation of the statistical average of velocity at a specific phase angle shows that the flow during upstroke phase angles remains more phase-locked. Nonetheless, the flow structures are consistently and characteristically present at each phase.

- From the comparison of flow in three span-wise locations, the results indicate that for the unswept airfoil, the mid-span of the airfoil surface has a higher degree of flow separation at the wing tip and the flow separation reduces towards the wing tip. The separation of flow from the airfoil surface also shows a higher degree of unsteadiness and less phase coherence at mid-span compared to the sections at 75% and 100% wingspan. This study showed that the phase-

40

coherence of the airfoil at a specific wing section and phase angle could be measured with Proper Orthogonal Decomposition to understand the phase coherence of pitching airfoil at a specific location and specific phase angle. As the sweep angle increases, the separation of flow shifts toward the wing tip. For sweep 15^0 wing, a higher degree of separation is observed at 75% wingspan compared to the other two sections at 50% and 100% wingspan. For further increase of sweep angle, small vortical separation during downstroke shifts more towards wing tip compare to sweep 15^0 and 0^0. In addition, the results indicate that for a higher sweep angle, the flow remains attached to the airfoil surface at a higher phase angle. The finding in this study is very consistent with the previous computational study [1, 2].

- Lastly, high Re number and comparatively less reduced frequency value affect the flow for unswept and sweep 15 wings. The results show that having less reduced frequency with respect to upstream flow advances the aerodynamics stall earlier compared to higher pitching frequency with respect to upstream flow conditions.

Although this study reveals that high 3D flow characteristics are involved with pitching finite-aspect ratio wings, a comprehensive tomographic study needs to be done to reveal the actual 3D shape of the vortical flow structures associated with pitching airfoil and to confirm the results obtained in the computational studies.

CHAPTER 4. A LIFETIME-PSP STUDY OF DYNAMIC STALL ON PITCHING SWEPT FINITE-ASPECT-RATIO WINGS

Chapter Abstract

An experimental investigation of moderate sweep on the three-dimensional dynamic stall of pitching finite-aspect-ratio wings was performed by fast response surface pressure measurement using lifetime method. The wings have an aspect ratio AR=4 and a NACA 0012 cross-section incorporated with rounded tips. Three airfoils with sweep angles, $\Lambda=0^0$, 15^0, and 30^0, were selected to investigate the pressure structure on the airfoil surfaces. The freestream flow conditions, such as Re=2x105 and Ma=0.1, were chosen to conduct the experimental study. The pitching motion of the wing is sinusoidal, between 4^0 and 22^0 angles of attack, and the experimental value of reduced frequency was set equivalent to k=πfc/U_∞ =0.1. The data was computed at specific phase angles during the upstroke (↑) and the downstroke (↓) of the pitching motion. The instantaneous and phase-average pressure maps are shown in this paper to describe the distinct patterns and vortex footprints on the wing surface. In addition, the standard deviation of the pressure map from a finite number of phase-locked instantaneous samples was calculated to exhibit the fluctuations of pressure structure from cycle-to-cycle at a specific phase angle.

Experimental Setup

To study the pressure distribution on the airfoil surface, A single shot lifetime method has been carried out. The experimental setup of the PSP campaigns are described in the following subsections.

<u>Airfoil Test Model</u>

For this experiment, two sweep angles 0º, 15º and 30º are used to perform PSP testing. The aluminum airfoils were machined using CNC machine with two holes running with the pitch angle;

one at 25% chord length and another 25 mm behind the first hole as shown in Figure 26. For unswept airfoil similar setup was designed in a CNC machine. It is important to note that to ensure free stream boundary conditions, the airfoil span has to be limited to half of the wind tunnel throat. This means the maximum span length of the airfoil will be approximately 152 mm or 6 inches. Both holes will be printed about the axis of symmetry.

(a)

(b)

(c)
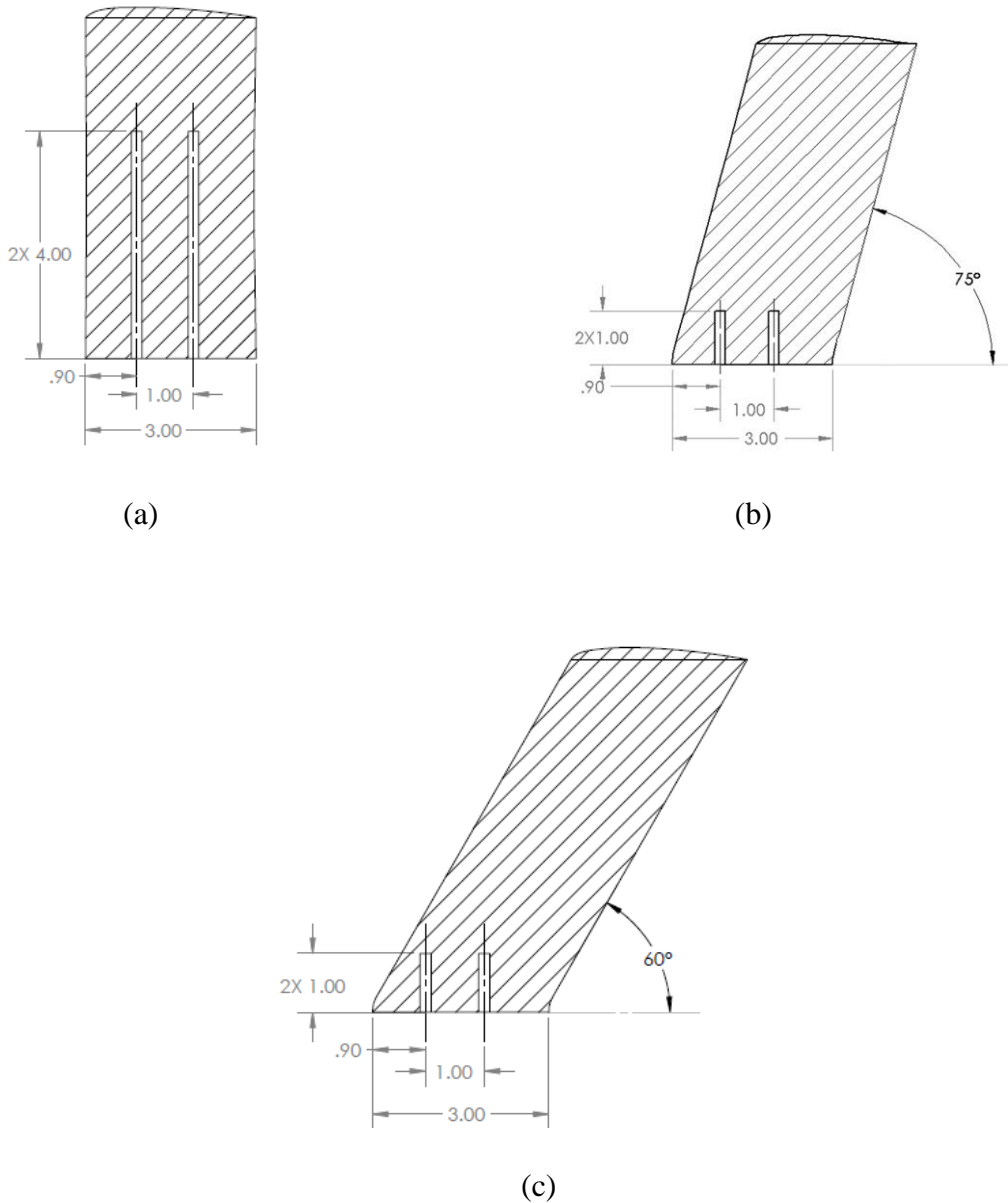
Figure 26. Dimensions and geometry for the NACA0012 airfoil with swept angle Λ = (a) 0º (b) 15º, and (c) 30°.

Wind Tunnel Setup

To simulate the pitching motion of the wing that is demonstrated in the computational study [1, 11], an apparatus capable of actuating sinusoidal motion was constructed in the NDSU machine shop. The entire unit was mounted to 80/20 aluminum rails rigidly below the wind tunnel such that the whole setup could be moved in any relative direction. The airfoil was fixed to a column such that it can rotate freely along its center axis. The actuation rod behind the center axis was attached to an actuating linear shaft. This shaft moves along a set of linear bearings to keep it on track. A counterweight and connecting arm were machined out of aluminum and arranged in a crankshaft formation to produce a sinusoidal action. At the center of the counterweight, a UL 12V DC motor capable of delivering up to 3000 RPM was mounted on a rigid support. The connecting arm is located 15 mm radially away from the center of rotation to produce a maximum stroke of 30 mm. The counterweight was made out of stock aluminum and intended to possess a high moment of inertia in order to maintain stability at high frequencies. To achieve greater dynamic balance, half of the counterweight was machined off on one side to counteract the moment applied by the weight of the rod and any loads induced by the airfoil.   The entire fixture is surmounted to a thick piece of aluminum connected to a platform adjacent to the wall of the wind tunnel.

Fixed to the end of the linear shaft, a rose joint is travelled freely on another shaft called the pitching arm. The pitching arm is connected to the rods inserted into the airfoil and then protruded through the acrylic insert. Though the model does deliver above the necessary parameters, it still produces a considerable amount of transverse vibration due to the unbalanced dynamic load. Figure 27 shows photography of the actuator assembly (a) and of the airfoil while pitching (b).
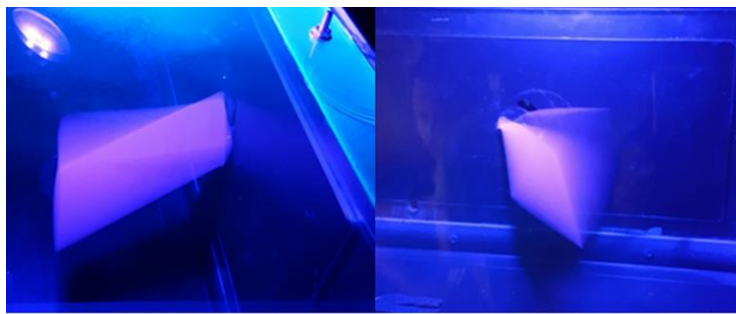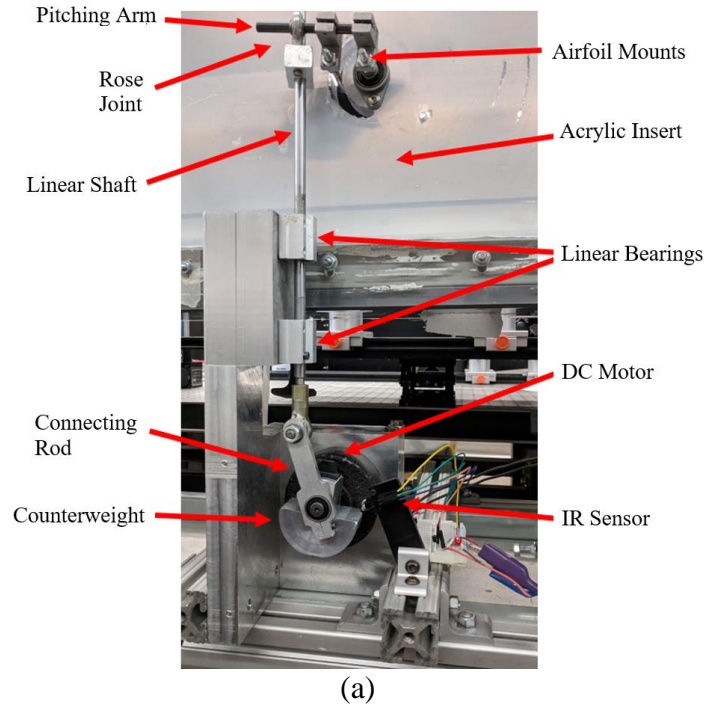
Figure 27. (a) Entire actuator assembly (b) images of airfoil pitching in the wind tunnel.

Test Conditions

In this experiment, the airfoil pitching frequency was set to 15 Hz. The corresponding reduced frequency (*k*) value is 0.1. The chord length of the airfoil was 3 inch, and the corresponding Reynolds number is approximately 2x105. The freestream Mach number is equal to 0.1.

Table 1. Test parameter for pitching airfoil cases.

Airfoil aspect ratio, AR	4
Airfoil chord, c	76.2mm/6inch
Freestream velocity, U	36.5 m/s
Freestream dynamic pressure, P_{dyn}	840 Pa
Reduced Frequency, k	0.1
Freestream Mach number, M∞	0.1
Chord Reynolds number,Re_c	$2x10^5$

Fast Porous Pressure-Sensitive Paint

Pressure-sensitive paint formulations consist of an oxygen-sensitive fluorescent dye and a binder for physically attaching the dye to the model surface. Due to the porous formation, the effective surface area is greater compared to the conventional binary paint. Due to the larger effective area, the signal-to-noise ratio is significantly higher. Therefore, it is possible to evaluate unsteady pressure in many aerodynamic applications using fast porous pressure-sensitive paint. In this experiment, the fast-porous pressure-sensitive paint is consisting of three parts [36] . Part A and B were mixed to provide the base layer coating, which works as a binder material. After 2 hours of curing at room temperature, Part C, a luminophore, was applied on top of the mixture of Part A and B.

Single-Shot Lifetime Method

To obtain an instantaneous pressure map, a single-shot lifetime-based method is deployed, as shown in Figure 28. In contrast to the conventional radiometric approach described in the previous subsection, a two-gate lifetime method obtains the time integral of two exposure gates,

which take counts of the luminescent decay of an oxygen-sensing fast porous paint [28, 36] . A combined double-pulse with a short duration of ~ 10 nsec from the 532 nm double-head Nd:YAG laser is used as a light source. The Q-switch of both laser beams was set at a certain value near the maximum power so that both pulses are emitted at the same time and they work as a single powerful light beam. The oxygen-sensing molecule returns to the ground state by decay through the oxygen quenching mechanism [28]. The lifetime decay of paint is then a function of the local absolute pressure which is proportional to the partial pressure of the oxygen. The decay time of this fast paints is in the order of microseconds as a function of the pressure, with faster decay at higher pressures, effectively mapping the pressures at the different locations imaged. The photo decay of paint through the oxygen quenching process in both wind off and wind on conditions was captured with a standard double frame PIV camera. The laser beam was triggered just before the first exposure of the camera ends. The laser trigger and camera exposure are selected to get optimized light emission between both gates. The ratio of both gates provides the intensity of wind off and wind on based on equations (1) and (2).

$$\frac{I_{windoff}}{I_{windon}} = \frac{\left(G_2/G_1\right)_{windoff}}{\left(G_2/G_1\right)_{windon}} \tag{1}$$

$$\frac{I_{windoff}}{I_{windon}} = A + B\,\frac{P_{windon}}{P_{windoff}} \tag{2}$$

Here A and B are calibration coefficients. The standard coefficients provided and evaluated by ISSI [36] were used in the experiment.
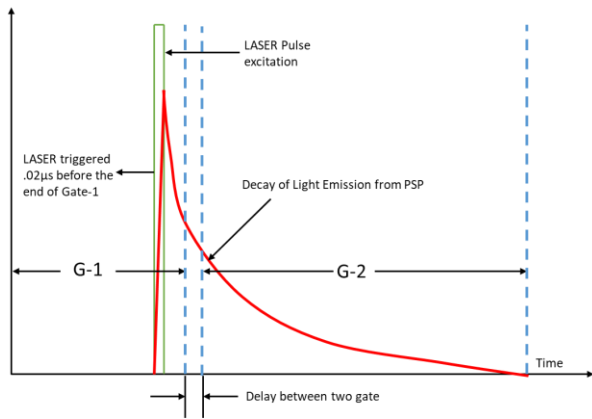
(a)   (b)
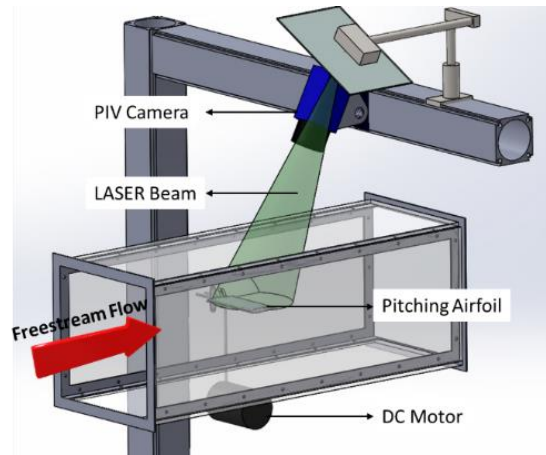
Figure 28. (a) Single-shot lifetime method schematic [15] and (b) Single-shot lifetime method setup using a Nd:YAG Laser and double frame camera.

Comparison between Pressure Tap and PSP Data

In this section, the data obtained from PSP and pressure tap campaigns are discussed. The comparison of Cp obtained from PSP and pressure tap scanner shows some representative phase angles of upstroke and downstroke in Figure 29 and Figure 30, respectively. The error bar in the pressure scanner data is shown based on the standard deviation computed from the 60 phase-locked instantaneous sample data points. The Cp curves from the PSP campaign are drawn from an ensemble average of 18~20 instantaneous samples along with a selected instantaneous frame that was processed for a specific case. As shown in Figure 29, the results show that at low phase angles, the pressure tap values at discrete points are very close to the Cp values obtained from the PSP campaign (Figure 29-a,b). As the phase angle increases to 17° and 19°, in Figure 6 (c,d), the Cp value obtained from PSP camping is under-predicted compared to the pressure tap scanner. However, the Cp curve from the instantaneous frame of the PSP experiment follows the change of pressure trend closely compared to the average Cp. For downstroke phases, the pressure coefficient values from the PSP campaign are closer to the pressure tap scanner at 11° and 13°. With the increase of phase angle, the deviation of Cp curve is observed in Figure 30 (c,d)

48

The inconsistencies between PSP data and Pressure tap scanner data reveals that in-situ calibration of PSP could be used. Another reason for discrepancies is the wind tunnel excursions during testing and the fact that the pressure signal is on the low end for the PSP detectability. Nonetheless the trends and surface patterns during unloading are clearly captured. As previous studies show that pitching airfoil exhibits a highly unsteady phenomenon, it is imperative to generate the calibration coefficients from the lab test conditions for the case of highly unsteady and separated flows. This will improve the quantitative quality of PSP data by reducing the offset observed. However, the PSP data captures very dynamics during stall characteristics from pitching airfoil. Another aspect that needs to be improved is to compute large samples of PSP data. As the unsteady nature of the flow associated with pitching airfoil is very high, so the small sample number from the PSP campaign may cause the deviation from the pressure tap scanner.
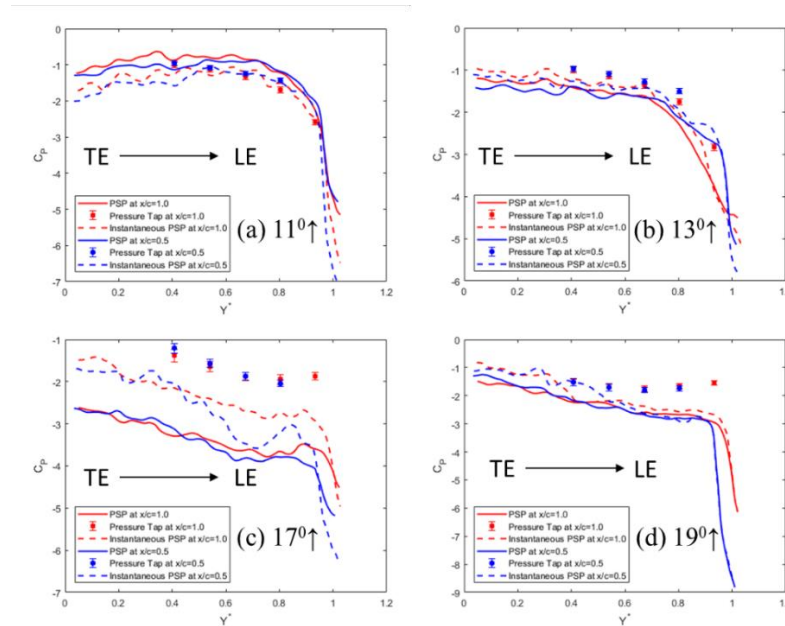
Figure 29. Comparison of PSP data (phase average) with pressure tap (phase average) for upstroke phases (Unswept airfoil).
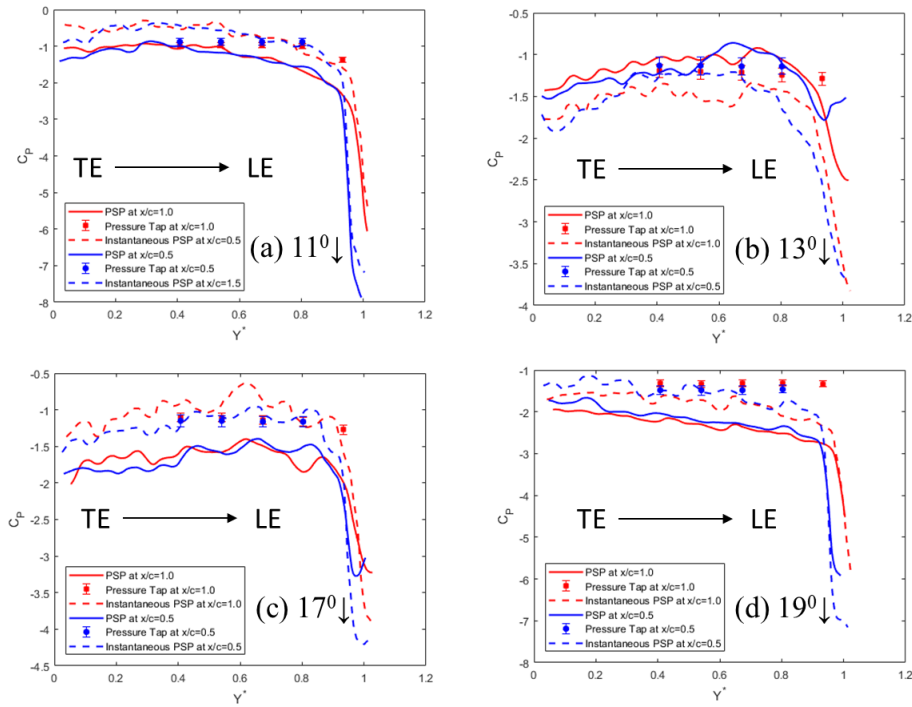
Figure 30. Comparison of PSP data (phase average) with pressure tap (phase average) for downstroke phases (Unswept airfoil).

Results and Discussion

Flow over Unswept Airfoil

In this section, one sample of instantaneous pressure contour from each phase angle during upstroke (↑) of the pitching cycle is shown in Figure 31. The data was captured at Re=2x10^5 and reduced frequency, k=0.1. At first, in the PSP processing, the pressure was computed, and then it was non-dimensionalized with respect to freestream pressure and dynamic pressure. The scale of the Cp of the instantaneous pressure for upstroke phase angles kept the same distinction of pressure map among the various angles during the upstroke cycle. In Figure 31 (a and b), corresponding to the upstroke phase, at phase angle 11° and 13°, the flow remains attached, and a small suction region appears in the very LE of the airfoil. The suction region indicates the existence of laminar separation bubble (LSB) in the flow during upstroke of the pitching. With the increase of phase angle, the uneven distribution of pressure also becomes more pronounced. In Figure 31 (c,d, and

e), at phase angle 15°, 17°, and 19°, the suction pressure increases, and the high-pressure region concentrates more towards the TE of the airfoil. The building up of suction pressure can be explained from the previous study [15, 16]. The early PIV studies [15, 16] show the formation of burst of LSB, which later evolves to a dynamic stall vortex (DSV) and their varying integral size along the span of the airfoil. The appearance of the DSV and their varying size along the span of airfoil contributes to the three-dimensionality of pressure distribution. As the phase angle increases to 21°, the pressure fluctuation structure indicates the complete separation of the flow, and some small negative pressure zones over the airfoil surface may indicate the formation of many secondary small vortices on top of the airfoil surface, which contribute to such disoriented pressure distribution at Figure 31 (f). In Figure 31, a comparatively low-pressure region appears near the end of the wing tip at all the phase angles. The formation of such a low-pressure zone is because of the formation of a TE vortex, which is also found in computational studies [1, 11, 13, 25, 37].

From the observation of the instantaneous plot, the results show a mild degree of aperiodicity during the upstroke phase of the pitching cycle. Due to the nature of the flow, the statistical average and standard deviation of upstroke phases of the pitching cycle need to be investigated, which will help understand the flow variation from cycle to cycle at a specific phase angle. The statistical phase-average and standard deviation are calculated from 18~20 various instantaneous samples. At first, the average contour of the pressure coefficient is shown in Figure 32. The phase-average pressure contour shows a consistent phenomenon of pressure similar to instantaneous plots. The growth of suction pressure in the LE is very consistent with the increase of phase angle. At phase angle 21°, in Figure 32 (f), the average pressure map washed out the small pressure structure that appears on the airfoil's surface. This happens due to the instability and unsteady nature of the vortices forms in the separated flow structures.
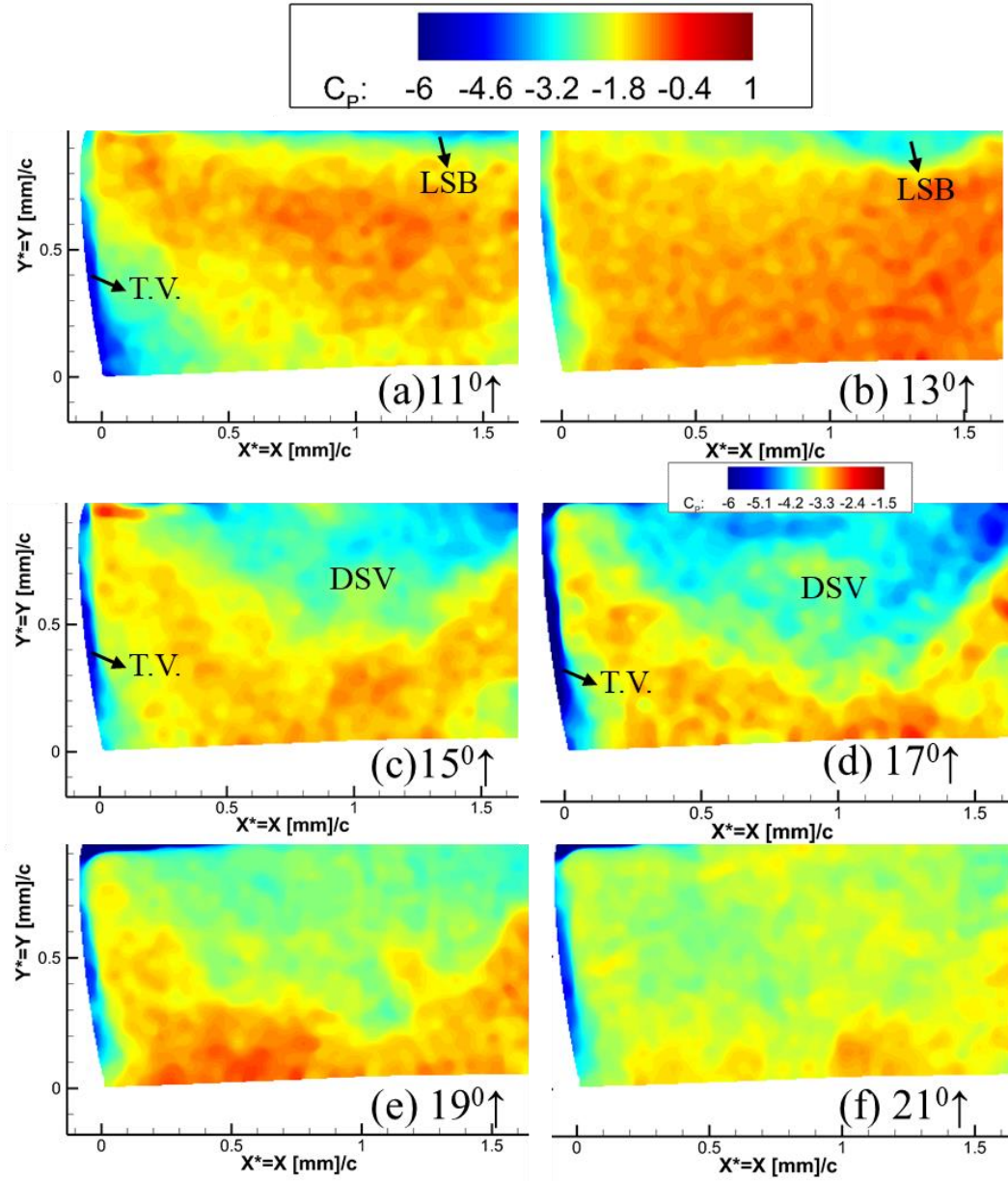
Figure 31. Instantaneous Pressure map for unswept airfoil at various angles during the upstroke.
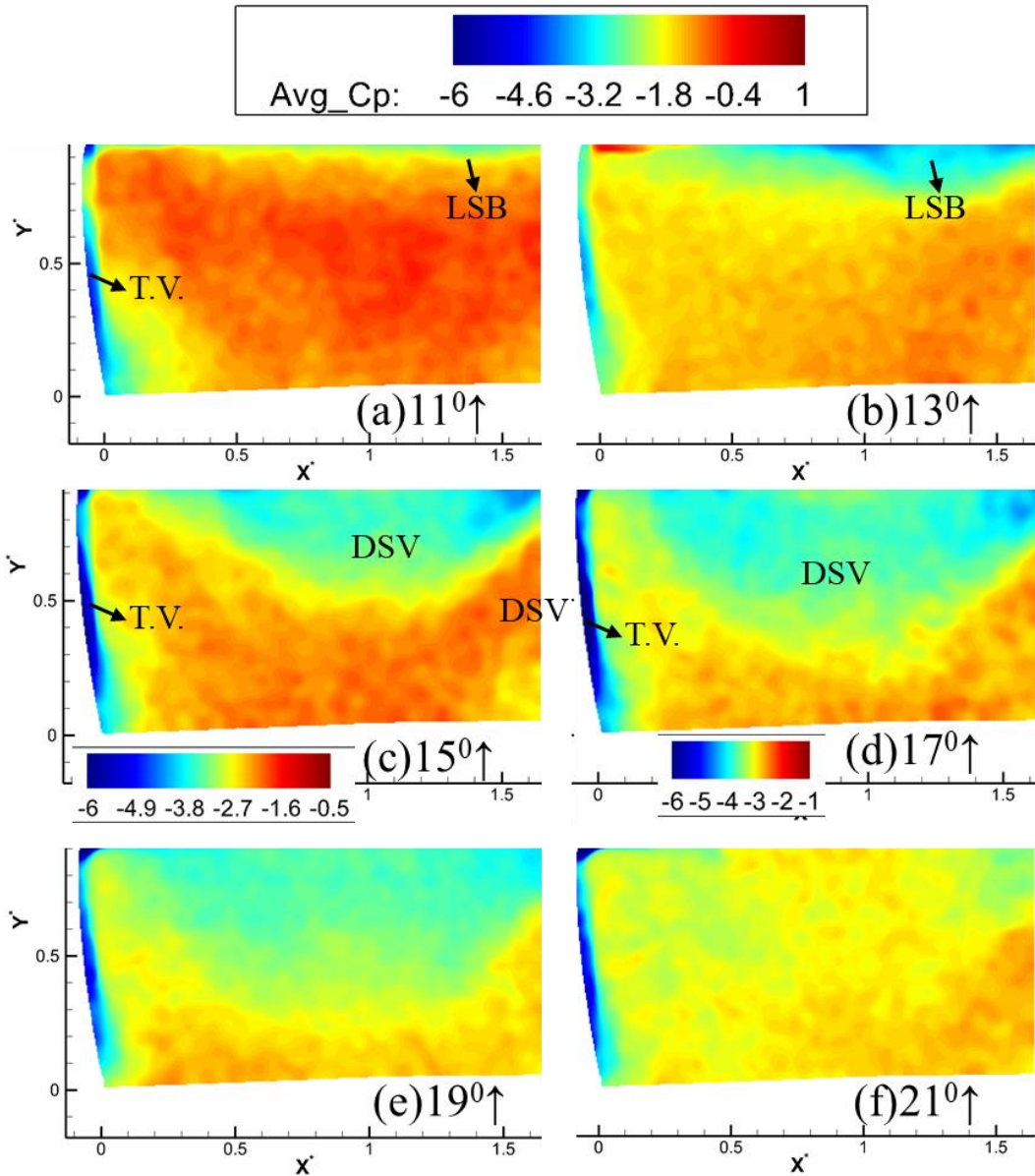
Figure 32. Average Pressure map for unswept airfoil at various angles during the upstroke.

The standard deviation of the pressure contour indicates the fluctuation of pressure varies from cycle-to-cycle. The standard deviation is shown in Figure 33 as a non-dimensional form. It was non-dimensionalized with dynamics pressure ($1/2$ ρU^2) of freestream flow. The standard deviation in Figure 33 shows some degree of pressure fluctuation at a low phase angle. At 21° phase angle, Figure 33 (f) shows the highest degree of pressure variation. This further confirms

the unsteady nature of flow at a higher phase angle. At low phase angles, such as in Figure 33 (a-e), show a small degree of fluctuation over the airfoil surface.

Figure 33. Standard deviation of pressure map for unswept airfoil at various angles during the upstroke of pitching cycle.

Generally, the flow structures at downstroke phases are more complex and aperiodic in nature. The instantaneous plot of downstroke phases is shown in Figure 34. As the downstroke flow structures are entirely different from the upstroke, the Cp is adjusted to a slightly different scale to exhibit the contrast in pressure contour of flow structures at downstroke phases. The data

54

was shown for phases of 11° to 21° at every 2^0 increments of phase angle, similar to upstroke cases. In Figure 34 (a and b), the pressure structure on the airfoil surface shows mild and non-uniform pressure distribution at low phase angles. However, for those corresponding phase angles (Figure 34 -a,b), the TE region shows a small pressure variation. This happens due to the separation that occurs at TE at 11° and 13° pitching down phase. With the increase of phase angles to 15°, 17°, and 19°, in Figure 34 (c,d, and e), the large uneven pressure distribution is observed due to massive flow separation. These separation flow structures are aperiodic and very unsteady from cycle-to-cycle. At 21° phase angle, in Figure 34 (f), a small negative pressure region occurs, which proves the formation of a secondary stall vortex on top of the dynamic stall vortex at higher phase angles. The results in downstroke phases are consistent with the previous experimental study reported at a similar Re number and reduced frequency value [15].

From the computed instantaneous frames of pressure contour, the ensembled average and standard deviation are calculated. The average Cp distribution is shown in Figure 35. The average of the pressure at phase angles does not show a distinct dominant pattern from the cycle-to-cycle. This may happen due to the lack of a large number of sample data and aperiodicity of flow from cycle-to-cycle.
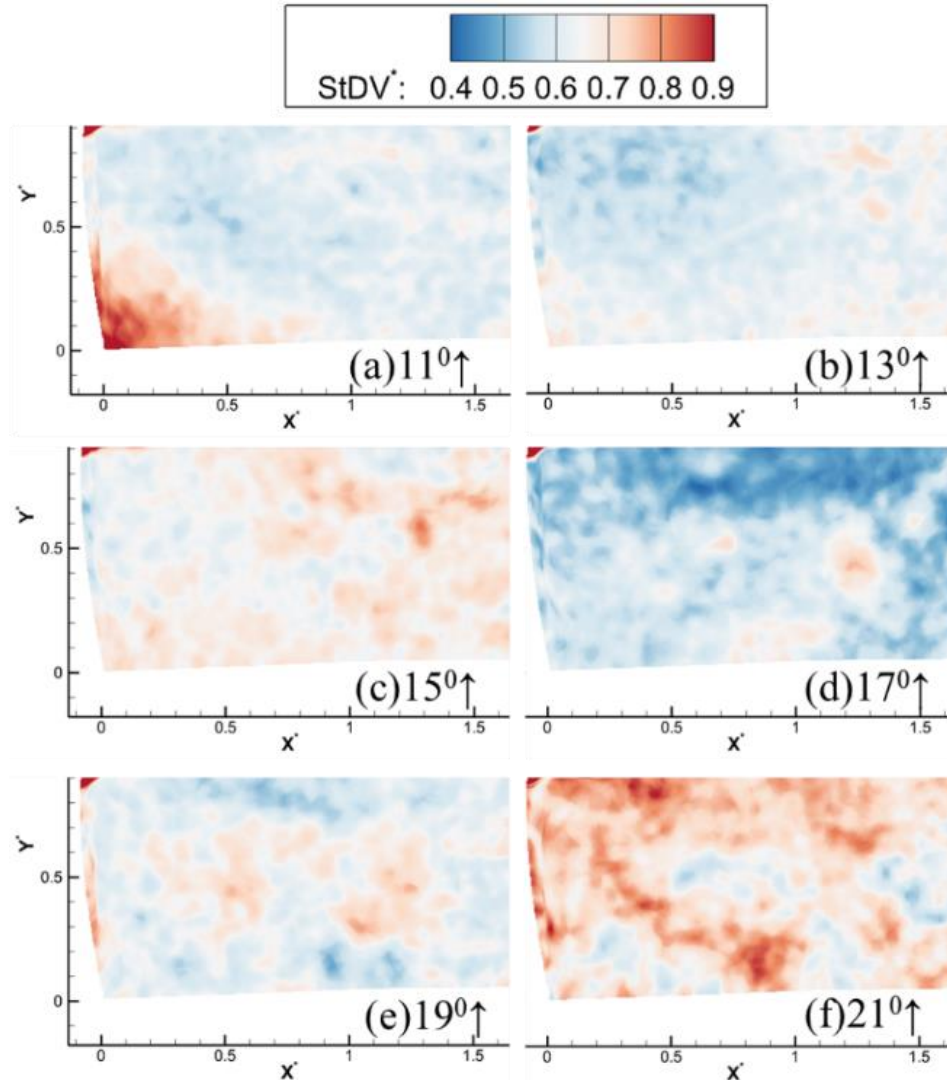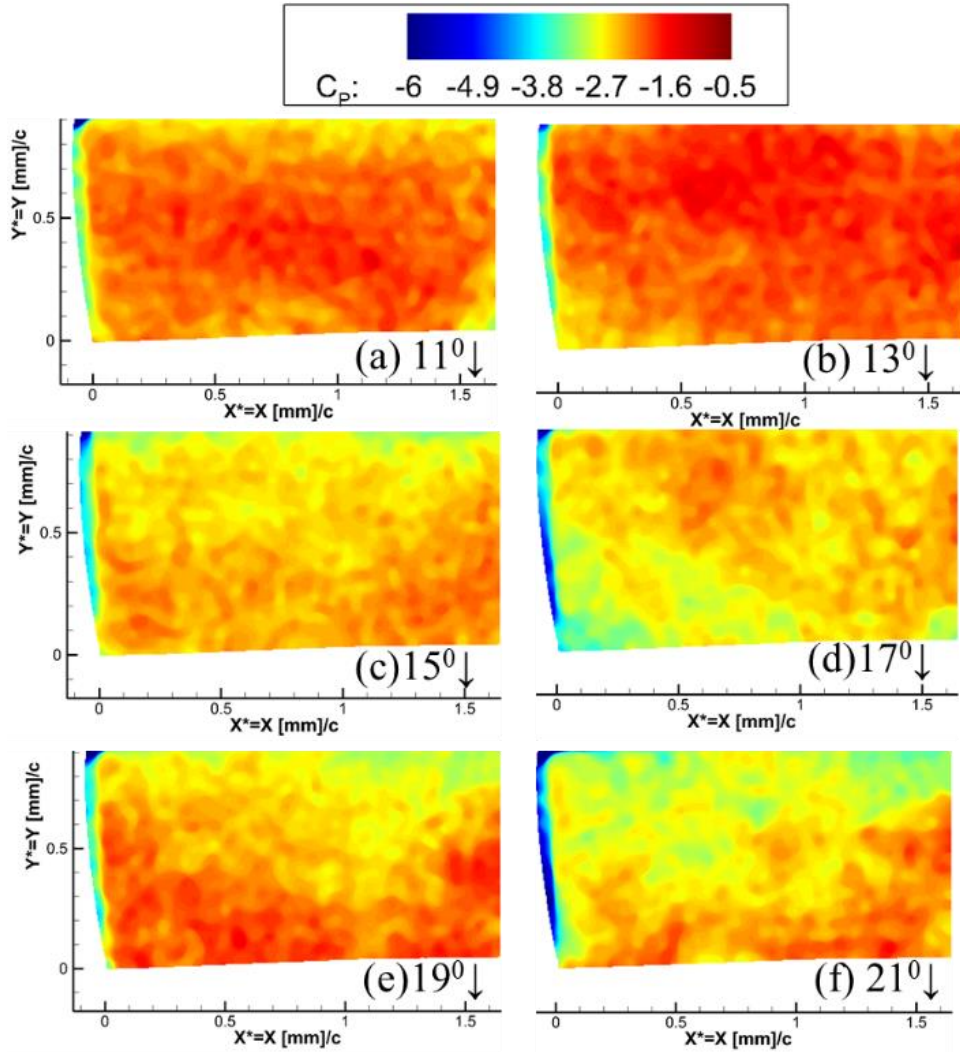
Figure 34. Instantaneous Pressure map for unswept airfoil at various angles during the downstroke.
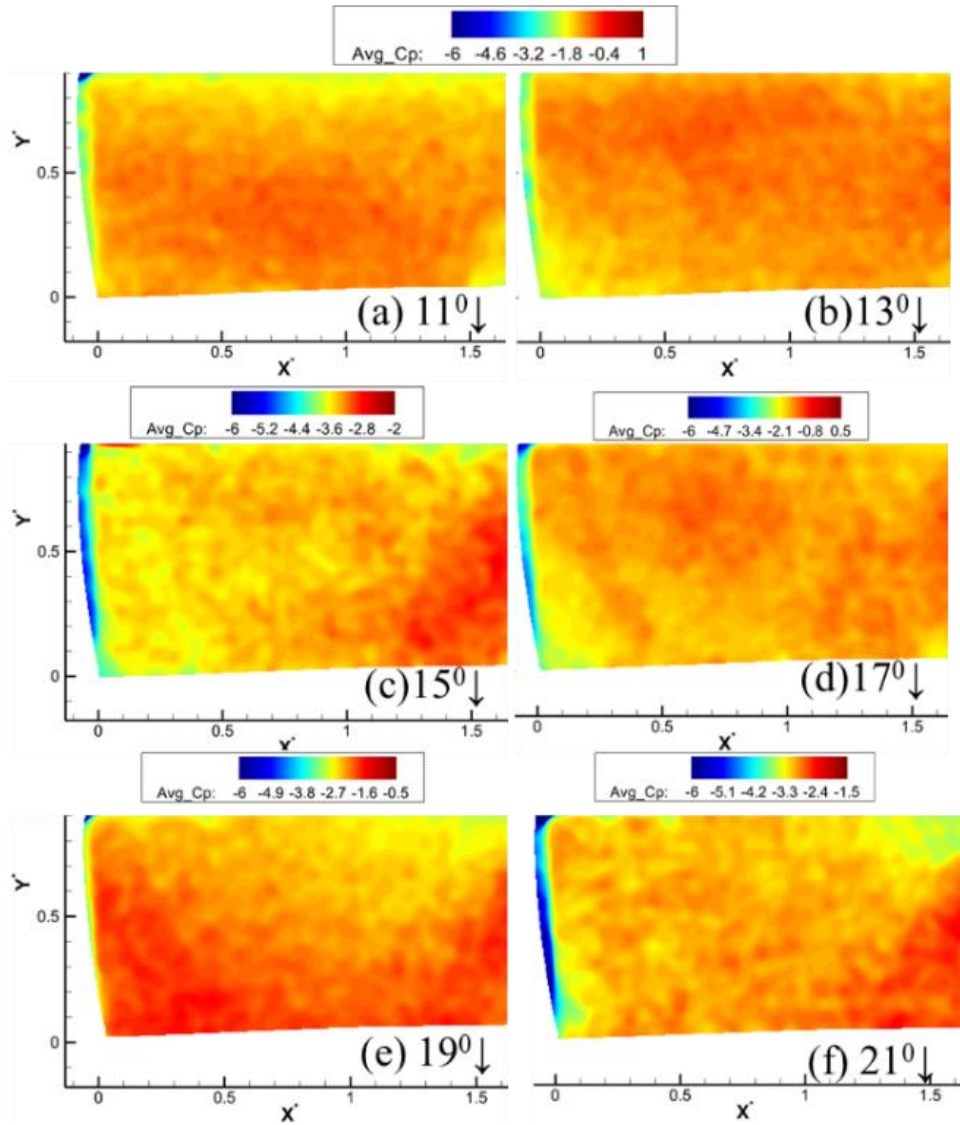
Figure 35. Average contour of various phase angles during the downstroke of unswept airfoil.

The standard deviation of downstroke phase angles is shown in Figure 36. The results indicate a higher value of fluctuation for different phase angles, even there exists no consistent patterns among the various phase angles.
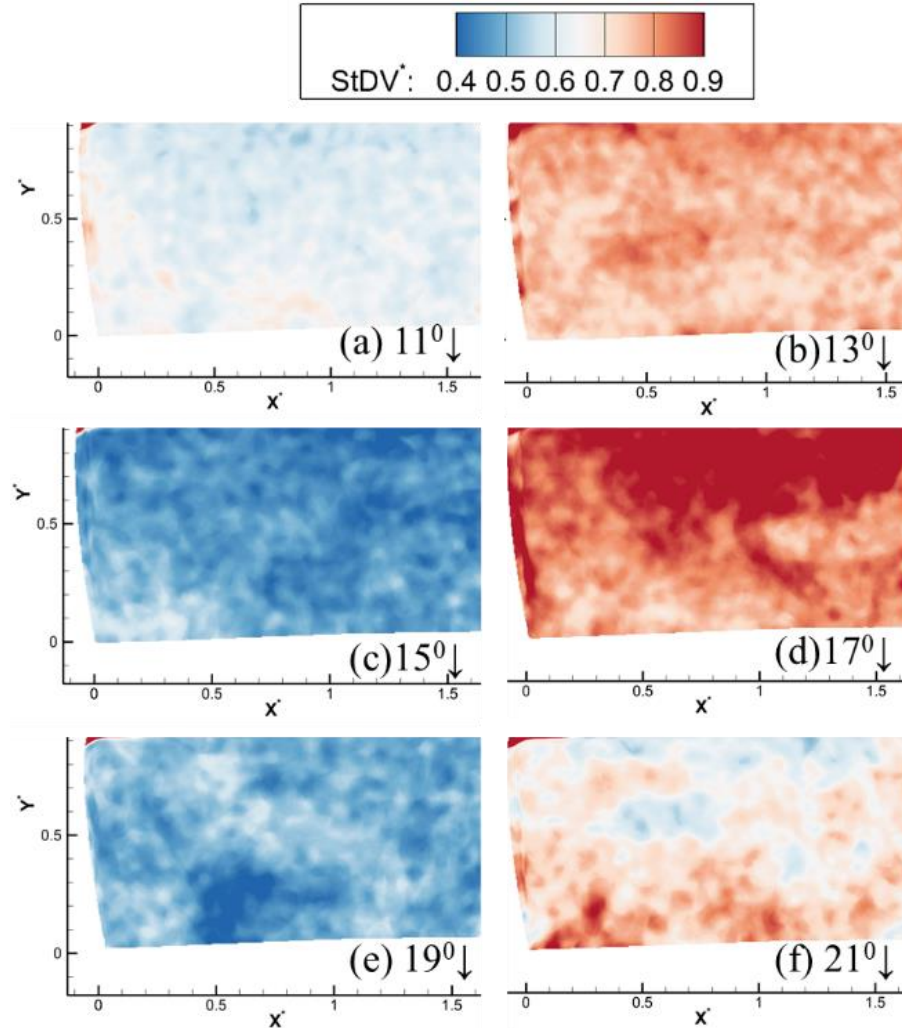
Figure 36. Standard deviation contour of various phase angles during the downstroke.

Flow over 15^0 Sweep Angle

The surface pressure map due to the evolution of flow structure for sweep 15^0 airfoil is shown in Figure 37 to Figure 40. During upstroke motion (↑) of the airfoil, the instantaneous pressure map at phase angles of 11^0, 13^0, 17^0, and 21^0 are shown in Figure 37 (a-d), and the average pressure map at those respective angles are shown in Figure 38 (a-d). During upstroke motion, a slight negative pressure region forms close to the LE of the airfoil. Unlike the unswept airfoil, the suction pressure due to the DSV shifts towards the wing tip with increased phase angles. As the suction pressure grows, the high-pressure region concentrates more towards the wing tip. As a

result, the pressure pattern towards the wing root becomes increasingly complex, and the wing tip vortex footprint remains similar to the unswept airfoil. At 21^0 ($\uparrow$), the DSV completely separates from the airfoil surface, and significant negative pressure on the airfoil surface builds up. The phenomenon of pressure fluctuation on the airfoil surface is very consistent during the upstroke of airfoil motion. As a result, the computed average pressure from 18 instantaneous frames shows the consistent result as instantaneous cases.

The flow structures are very complex and aperiodic in nature during downstroke for sweep 15^0 as well. The results, shown in Figure 39, indicate a high-pressure region on the airfoil surface. The high-pressure regions are 3-dimensional in nature. When the angle of attack during pitching motion is 21^0($\downarrow$), the negative pressure region exists, and with the continuation of downstroke motion, the flow starts to attach, and high pressure starts to become less 3-dimensional. The slight pressure structure indicates the existence of a secondary vortex on top of the airfoil surface. These vortices are shown in previous computational studies [10-14]. These small vortical structures are non-repeatable and aperiodic. Therefore, they get washed out in the average pressure map, as shown in Figure 40.
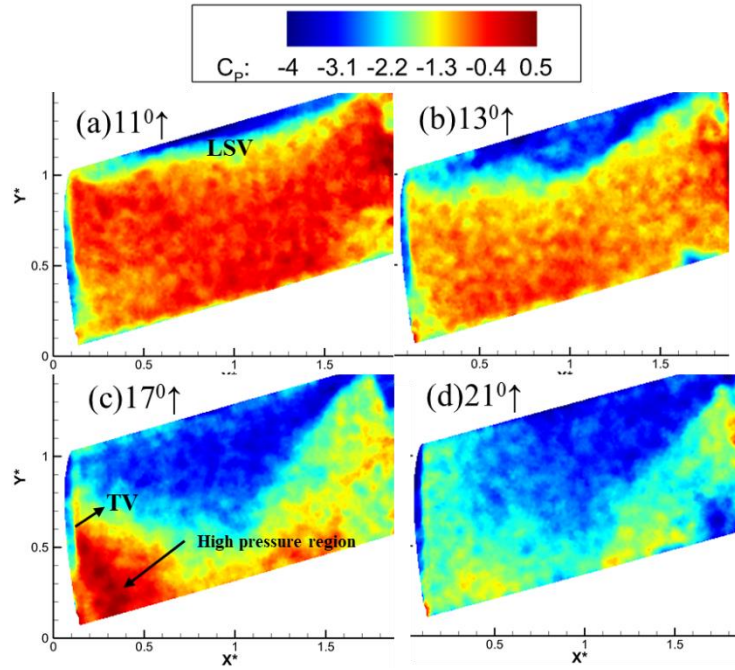
Figure 37. Instantaneous Pressure map for sweep 15^0 airfoil at various angles during the upstroke motion.
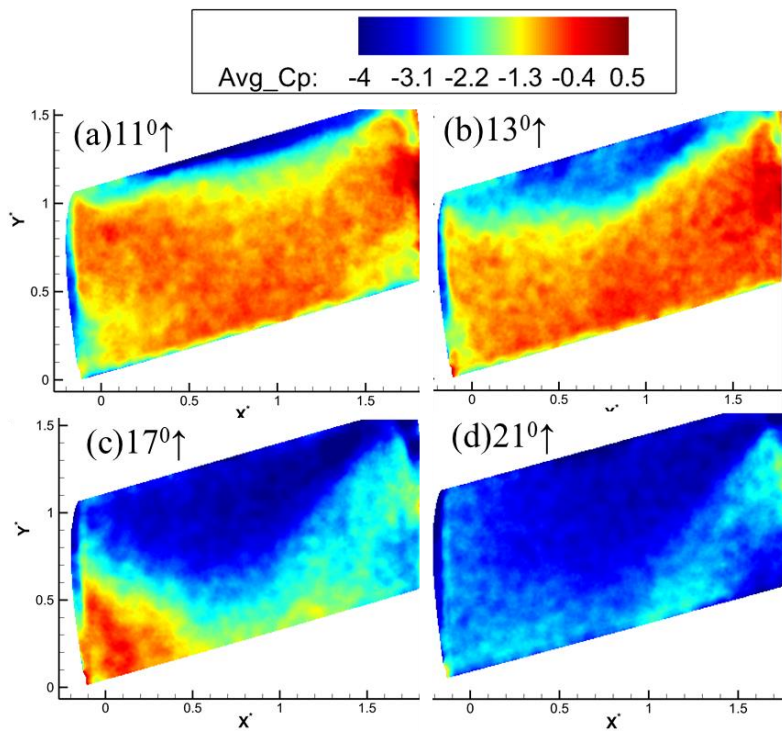
Figure 38. Average Pressure map for sweep 15^0 airfoil at various angles during the upstroke motion.
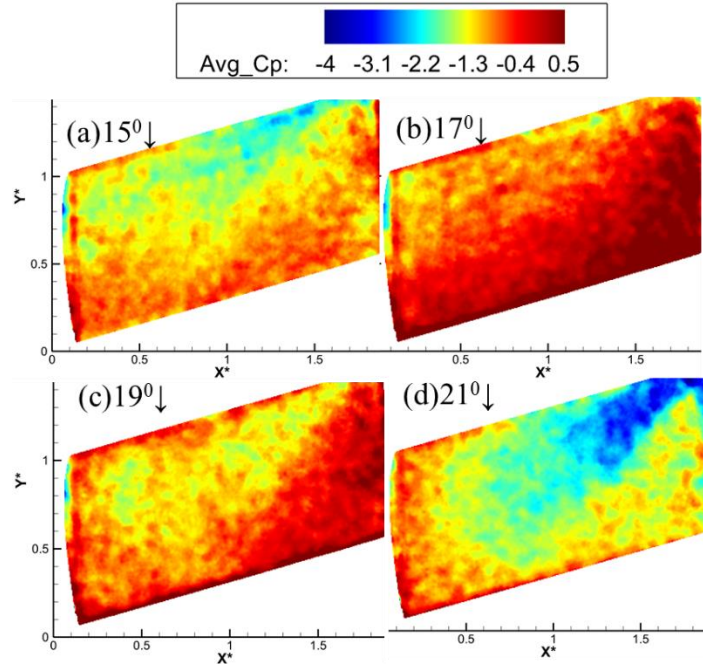
Figure 39. Instantaneous Pressure map for sweep 15^0 airfoil at various angles during the downstroke motion.

Figure 40. Average Pressure map for sweep 15^0 airfoil at various angles during the downstroke motion.

61

Flow over 30^0 Sweep Angle

 In this section, flow over a moderate sweep of 30° airfoil is investigated. Like the unswept and sweep 15^0 airfoil, the data was captured at various phase angles during the upstroke and the downstroke of the pitching cycle. The results are shown in Figure 41. At a low phase angle, the flow remains attached. The pressure is distributed over the airfoil surface almost uniformly with a small suction region formation in the LE of the airfoil. As the phase angle increase to 13°, 15°, and 17°, as shown in Figure 41, the suction pressure in the LE starts to builds up and proliferates towards the wing tip (outboard) compare to the wing root (inboard). At the edge of the wing tip, the low-pressure region indicates wing tip vortex formation at those phase angles. As the phase angle increases to 19°, as shown in Figure 41 (e), at the location of x*= 0.5 (approximately 39 mm from the wing tip), the high-pressure region in the TE region breaks down. A small pressure footprint appears that later evolves to a low-pressure region located diagonally over the wing tip region in Figure 41 (f). In Figure 41 (f), the pressure footprint shows similar characteristics as the footprint of the arch vortex obtained in the previous computational study [11, 12]. However, the representative case that is shown in Figure 41 (f) is not a repetitive phenomenon. This may happen due to the interaction between the wing tip vortex and the separated vortex and the unsteady flow phenomenon from cycle-to-cycle. For upstroke cases, the ensembled average is calculated from 19 instantaneous frames, shown in Figure 42. The average pressure contour shows a similar trend compared to instantaneous cases. However, the magnitude of the phase-average pressure contour varies from the instantaneous sample.
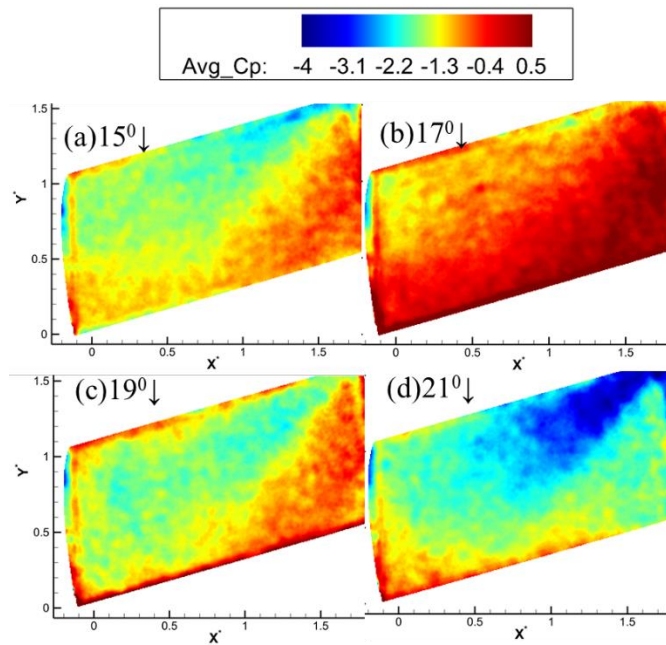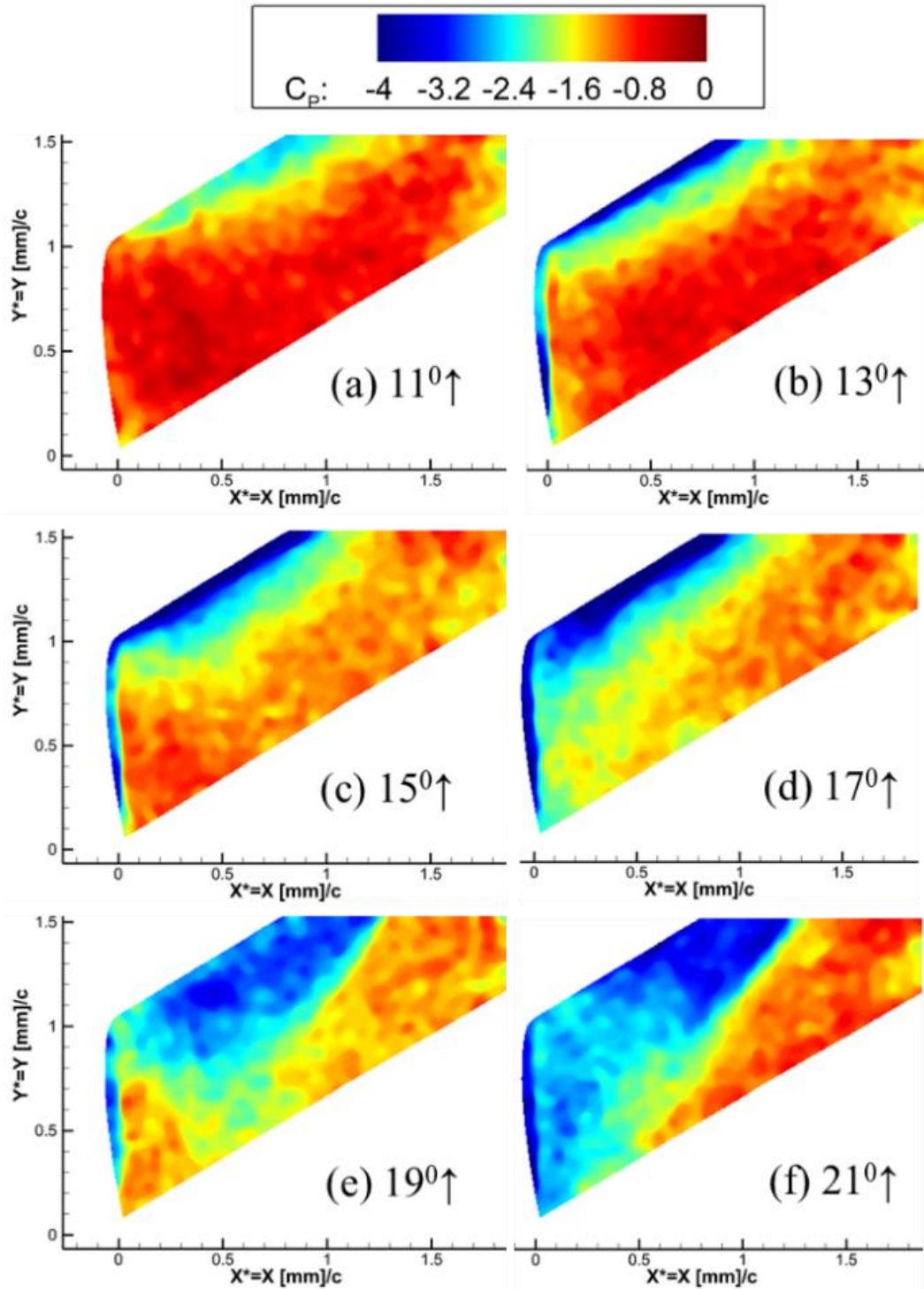
Figure 41. Instantaneous Pressure map for sweep 30⁰ airfoil at various angles during the upstroke.
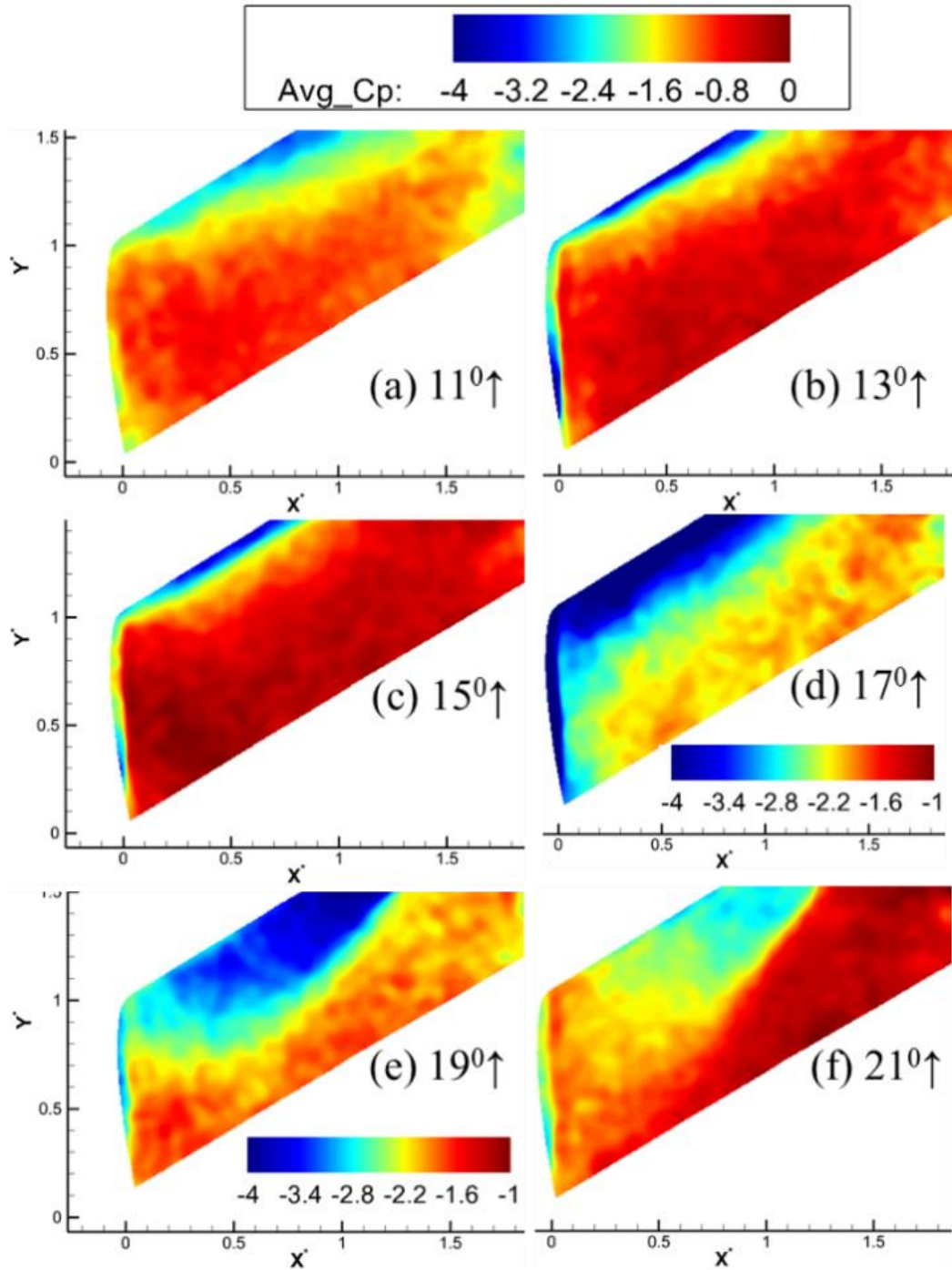
Figure 42. Average Pressure map for sweep 30⁰ airfoil at various angles during the upstroke.

The average pressure map also indicates the formation and growth of suction pressure is more towards the wing tip (outboard of the airfoil). This proves that as the sweep angle increases,

the formation of separation vortices forms consistently towards the wing tip (outboard of the airfoil) even though their shape and characteristics vary from cycle-to-cycle. In the average pressure map, small structures in the LE and TE washes out.

For sweep 30°, the downstroke phases are presented in Figure 43. The pressure contour shows a high-pressure region towards the wing root or inboard of the airfoil. With the increase of phase angle, the higher-pressure region towards the inboard (wing root) collapses and concentrates more towards the outboard (closer to wing tip), as observed in Figure 43 (a-d). At 19°, before reaching to maximum phase angle, a low-pressure region appears in one sample case. This may happen due to the strong interaction between the tip vortex and the stall vortex. As the phase angle reaches 21° and 22° (not shown here), the wing tip stall happens, and the high-pressure region appears at LE of the wing tip.

As mentioned earlier, the downstroke phases exhibit a higher degree of unsteady phenomenon and aperiodicity from cycle-to-cycle. The average pressure calculated from various samples show a similar trend. Some phase angles, such as $13^0, 15^0$, and 17^0, show large fluctuation towards the wing tip because the dominant flow structures vary at those representative phase angles. At a higher phase angle, the separation vortex remains consistent with the variation of the secondary vortex that contributes a lower value of standard deviation. To show the contrast of the pressure structure, the pressure contours are shown on their own scale in Figure 44.

Figure 43. Instantaneous Pressure map for sweep 30^0 airfoil at various angles during the downstroke.
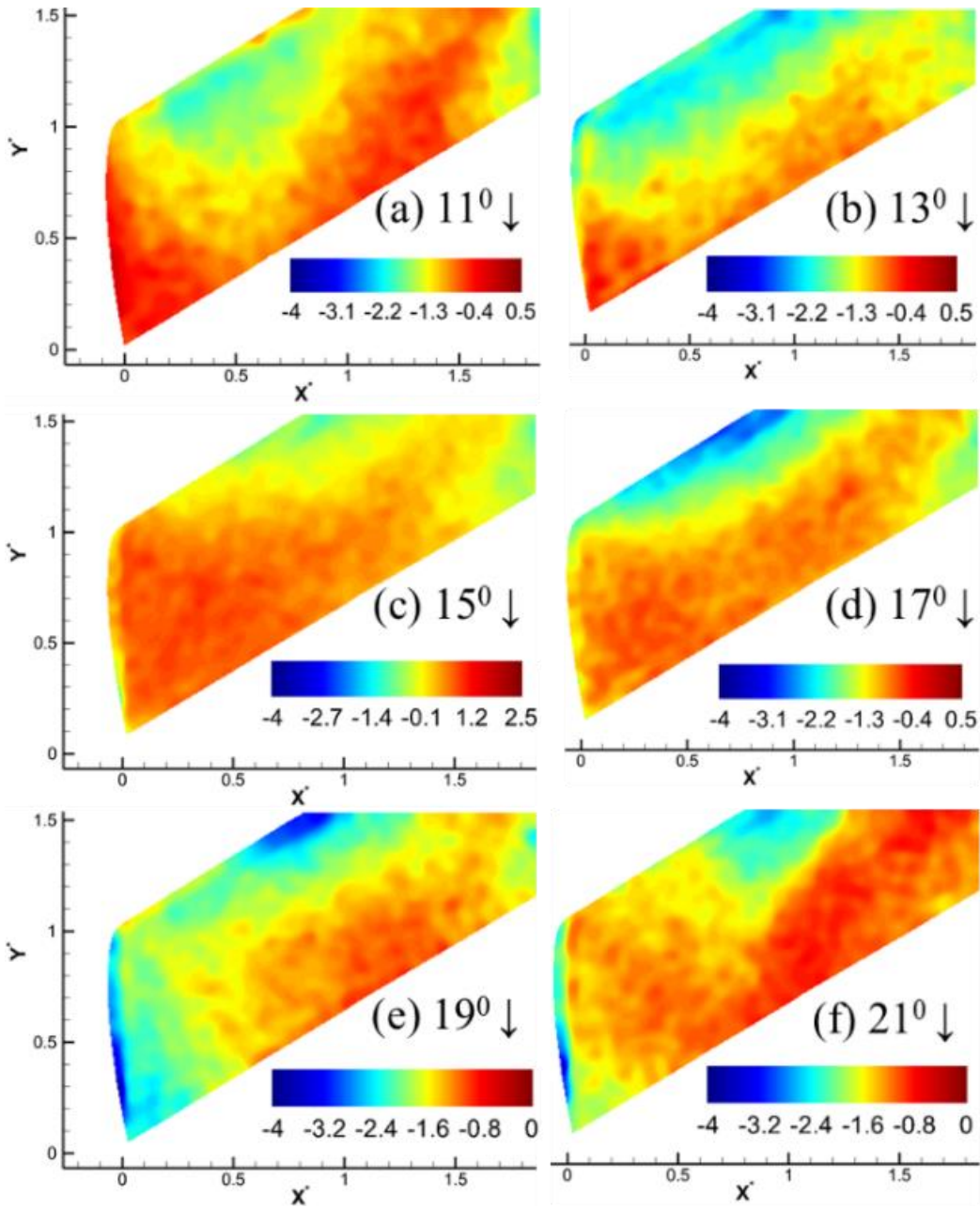
Figure 44. Average Pressure map for sweep 30⁰ airfoil at various angles during the downstroke.
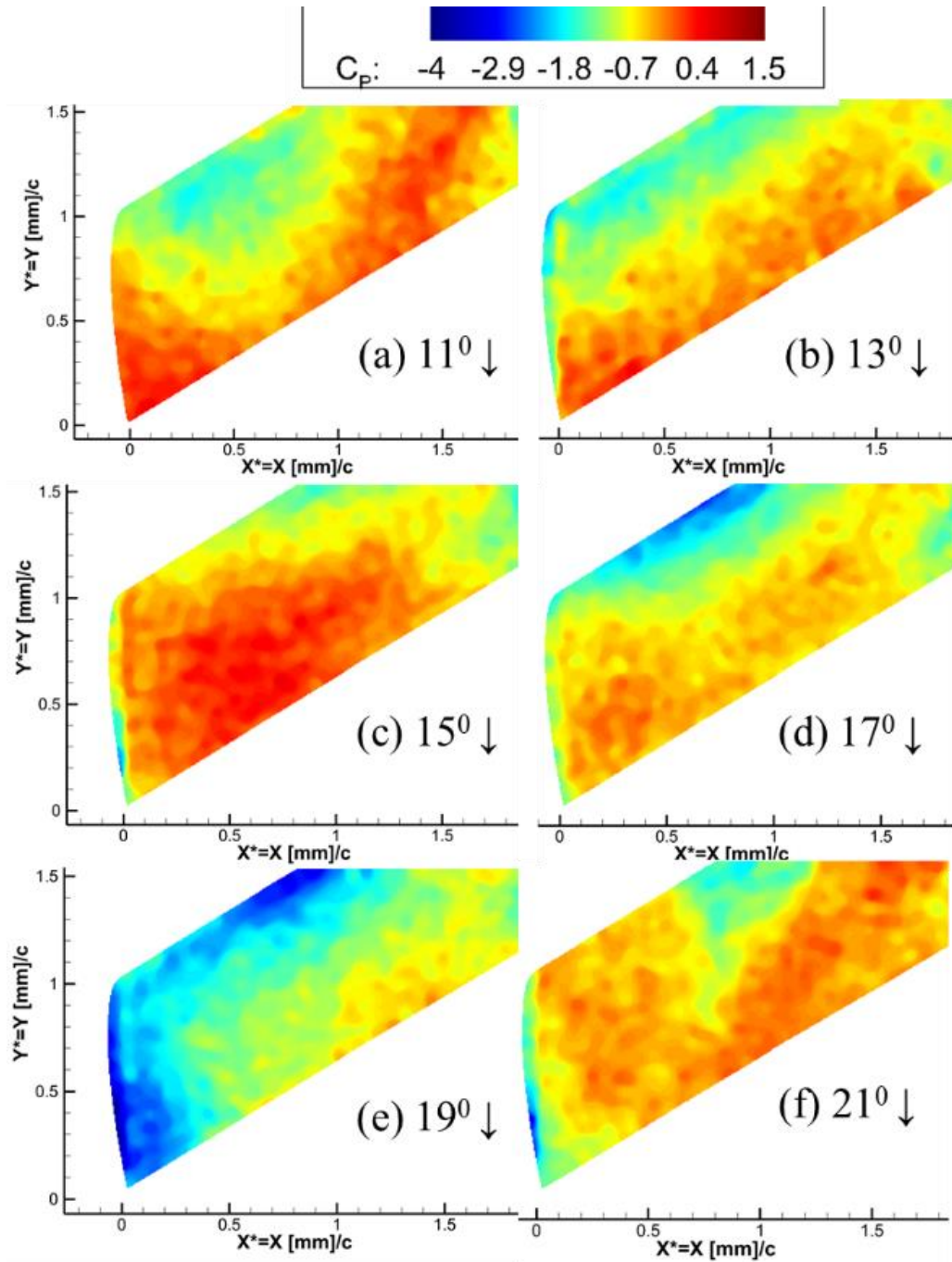
Figure 44. Average Pressure map for sweep 30^0 airfoil at various angles during the downstroke.

Chapter Summary and Conclusion

This study aimed at demonstrating the measurement of pressure measurement with fast porous paint to show the unsteady nature of dynamics stall associated with pitching-finite-aspect ratio wing and the effect of sweep angle. A laser-based, single-shot lifetime method with a high-resolution PIV camera was deployed to obtain enough signal to demonstrate the instantaneous pressure footprint of the vortex structures that forms during the pitching cycle of an airfoil. The test was conducted at a Reynolds number of $2\text{x}10^5$ and reduced frequency values k of 0.1. Three sweep angles, which are 0^0, 15^0 and 30^0, were selected to explore the change of dynamic stall behavior due to sweep angle change. A pressure tap scanner was later deployed to compare how the quantitative value obtained from PSP varies from pressure tap measurement. The insights obtained from the experiment and results are listed in bullet point as follows:

- The Cp value obtained from the pressure tap scanner and PSP campaign show a deviation. This deviation may occur due to a lack of test-condition calibration data and a small sample size from the PSP campaign. However, the obtained data shows a trend similar to pressure tap scanners and consistent with the previous studies. Besides, it also offers the motivation for future improvement of test conditions.

- The pressure topology obtained for unswept airfoil was shown for two-phase angles of upstroke and downstroke. The upstroke phases show the build-up suction pressure as the phase angle increases, and at stall condition, the pattern shows random turbulent characteristics. The consistent pattern of suction pressure and their variation is captured from the ensembled average and standard deviation plot. For downstroke phases, the flow is unsteady and more three-

dimensional in nature. The random pattern of the downstroke phases is captured from the selected instantaneous, average, and standard deviation pressure map.

- In the last two sections, the results were depicted for a moderate 15^0, and 30^0 sweep angle. The data shows that for upstroke phase angles, suction pressure builds up in the LE region. With the increase of phase angle, the suction pressure grows, and it grows more towards the outboard of the wing. This phenomenon is very consistent with the results that are reported in both computational and experimental studies. As the flow is very random and unsteady in nature, it shows a higher three-dimensionality for downstroke phases. In general, for downstroke phase angles, the high-pressure region concentrates more towards the wing tip. The ensembled average and standard deviation from a finite number of samples also show a similar trend.

- Overall PSP certainly captured periods of tip unloading during the cycle, but definitive imprints of the arch vortex legs are still not so clear. To that regard other motion profiles could be considered to track those better. Varying the rates and incidence amplitudes may provide more conclusive evidence of the motion-induced effects vs. measurement effects. With this lower pitch rate, the wing is subjected to higher angles of attack for longer durations in time than with the higher pitch rate used in the simulations [9-13]. Thus, it may be beneficial to reduce the maximum angle of attack when the lower pitch rate is used to achieve a similar response.

The PSP study is valuable for studying the unsteady flow, such as dynamics stall associated with pitching airfoil. This is important for developing better insight into flow phenomenon and

complex interactions of fluid and structures. However, significant developments are necessary to improve the quantitative measure of pressure by PSP. In the future, a calibration and test conditions needs to be developed that can overcome the extraction of quantitative pressure magnitude for largely separated and unsteady flow.

CHAPTER 5. DYNAMIC STALL STRUCTURES DURING PITCHING OF MODERATE SWEEP FINITE-ASPECT RATIO WING

Chapter Abstract

Based on the results obtained so far, it becomes evident that the sweep angle has an effect on dynamics stall during the pitching motion. The findings are also consistent with the recent computational studies. However, the existence of an arch-shaped vortex has not been found clearly for $Re=2x10^5$ and k=0.1. The visualization of arch-shaped-flow structure is very challenging using planner PIV due to its 3-dimensional characteristics. One way to show the existence of an arch-shaped vortex is to obtain its pressure footprint as it has unique features confirmed by the computational study. However, for $Re=2x10^5$ and k=0.1, the pressure map does not provide explicit confirmation of the existence of the arch-shaped vortex. Therefore, a further investigation has been conducted using the PSP technique described in Chapter 4 to confirm the presence of an arch-shaped vortex during pitching motion of finite aspect ratio wing. A sweep 15^0 aluminum airfoil was printed in a CNC machine that is capable of pitching with 30Hz. The flow parameters were matched precisely similar to the current computational study, which are $Re=2x10^5$, freestream Mach number, Ma=0.1, and reduced frequency, k=0.2. The computational study showed an arch-shaped vortex forms at the center for sweep 0^0, at the center of the half span for sweep 15^0, and towards the wing tip for sweep 30^0. As the experimental study was set up for half span and the center of the airfoil is very close to the wind tunnel wall, it is unattainable to obtain the characteristics of the arch-shaped vortex. For sweep 30^0, the high sweep angle makes it challenging structurally to pitch it at 30Hz so that the reduced frequency, k=0.2, matches at $Re=2x10^5$ and Ma=0.1. That's why from all the perspectives, the sweep 15^0 airfoil is selected to conduct the study at $Re=2x10^5$ and k=0.2. In addition, a PIV study was conducted to see the flow

structure at three spans of the airfoil. The experimental setup of the PIV and PSP setup is similar to the study conducted in Chapters 3 and 4.

Results and Discussion

The results were obtained for sweep 150 airfoils with the flow at Re=$2x10^5$ and reduced frequency, k=0.2. At first, a PIV experiment was conducted to obtain the qualitative and quantitative flow. The PIV data was taken at three spans of the airfoil. Then the PSP experiment was done to obtain the surface pressure structure. Similar to previous studies explained in chapters 3 and 4, the data was taken for both downstroke and upstroke motion. The results obtained at three critical angles, 21^0 upstrokes, 22^0 Max, and 21^0 downstrokes, are discussed from obtained PSP and vorticity and velocity data from the PIV campaign.

Some selected instantaneous pressure contour, velocity, and vorticity data were presented in Figure 45 to Figure 47. The velocity and vorticity plot obtained from the PIV campaign are shown at three spans. Three sections were shown as section A-A (midspan), B-B (75% span), and C-C (wing tip). When the phase angle reaches 21^0 during pitching up, the separation bubble formed in the leading edge of the airfoil breaks down, and a burst occurs at 75% of the airfoil. The burst is observable in Figure 45 (b, c) at the velocity and vorticity contour. The PSP data shows the LSB burst's footprint and the exact footprint of the arch-shaped vortex. The PSP data proves the theory of the existence of the arch-shaped vortex of recent computational study [11, 12, 17, 25, 26, 37, 38]. As the airfoil pitching continues and the phase angle reaches a maximum of 22^0, shown in Figure 46, the separation burst moves towards the trailing edge more and starts to detach from the airfoil surface. The pressure distribution of the flow becomes more complex in nature, and the magnitude of the pressure starts to change. The high-pressure regions start to concentrates towards the TE of the airfoil. As the airfoil starts to pitch downwards, the results at 210 pitching down are

shown in Figure 47, indicating that the vortex shedding from the airfoil surface. As the vortex shedding continues, the pressure distribution on the airfoil surface becomes complex and three-dimensional.

Figure 48 shows the average pressure distribution on the airfoil surface during the pitching motion. The average results indicate that at 21^0 pitching up, the formation of an arch-shaped vortex is consistent during the pitching motion of the airfoil. The two negative concentric pressure zone appears on the airfoil surface in the 50% to 75% airfoil span region. As the phase angle reaches 22^0 max, the pressure structures become complex, and the magnitude varies drastically from the phase angle of 21^0 pitching up due to the complete flow preparation. As the flow starts to pitch down, the pressure distribution starts to become more three-dimensional. Due to the aperiodic nature of the flow, the small secondary vortices wash away in average pressure contour.
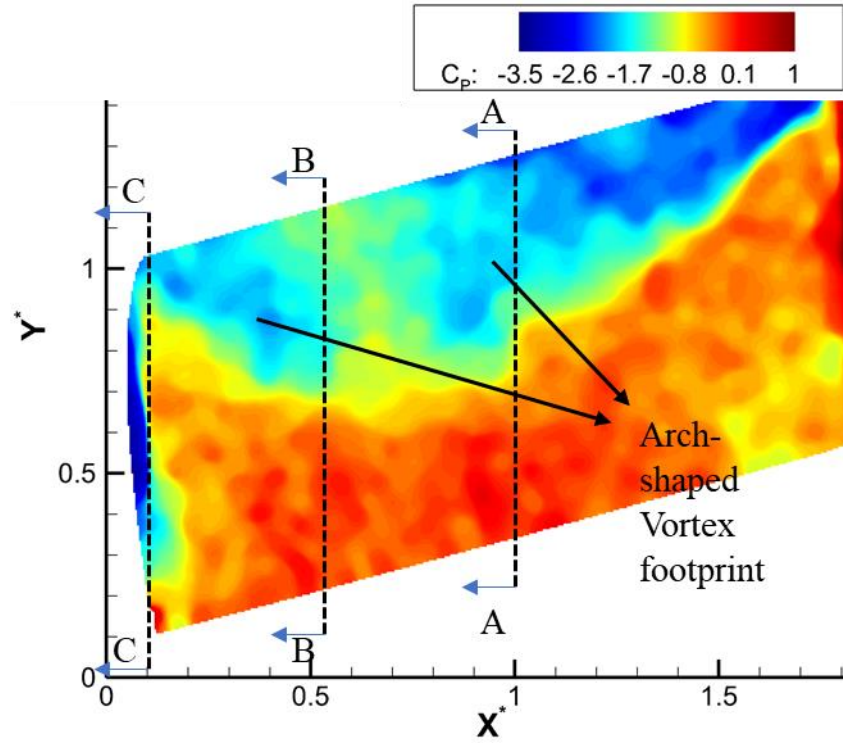
(a)
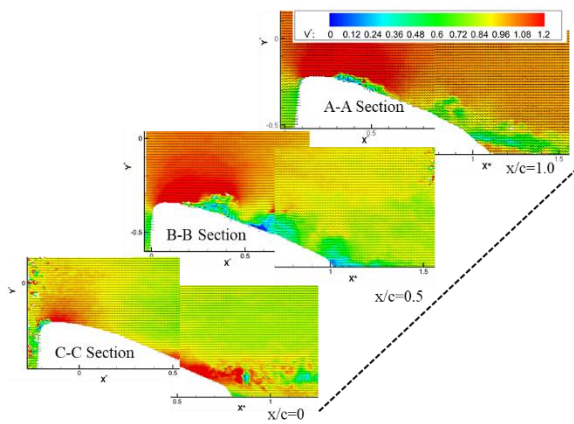
(b)
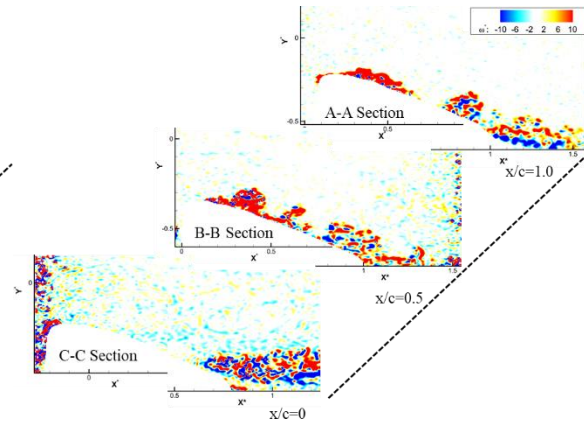
(c)

Figure 45. (a) Instantaneous pressure contour (b) instantaneous velocity map (c) instantaneous vorticity map for phase angle of 21^0 upstroke.

(a)

(b)   (c)

Figure 46. (a) Instantaneous pressure contour (b) instantaneous velocity map (c) instantaneous vorticity map for phase angle of 22^0 max.

(a)
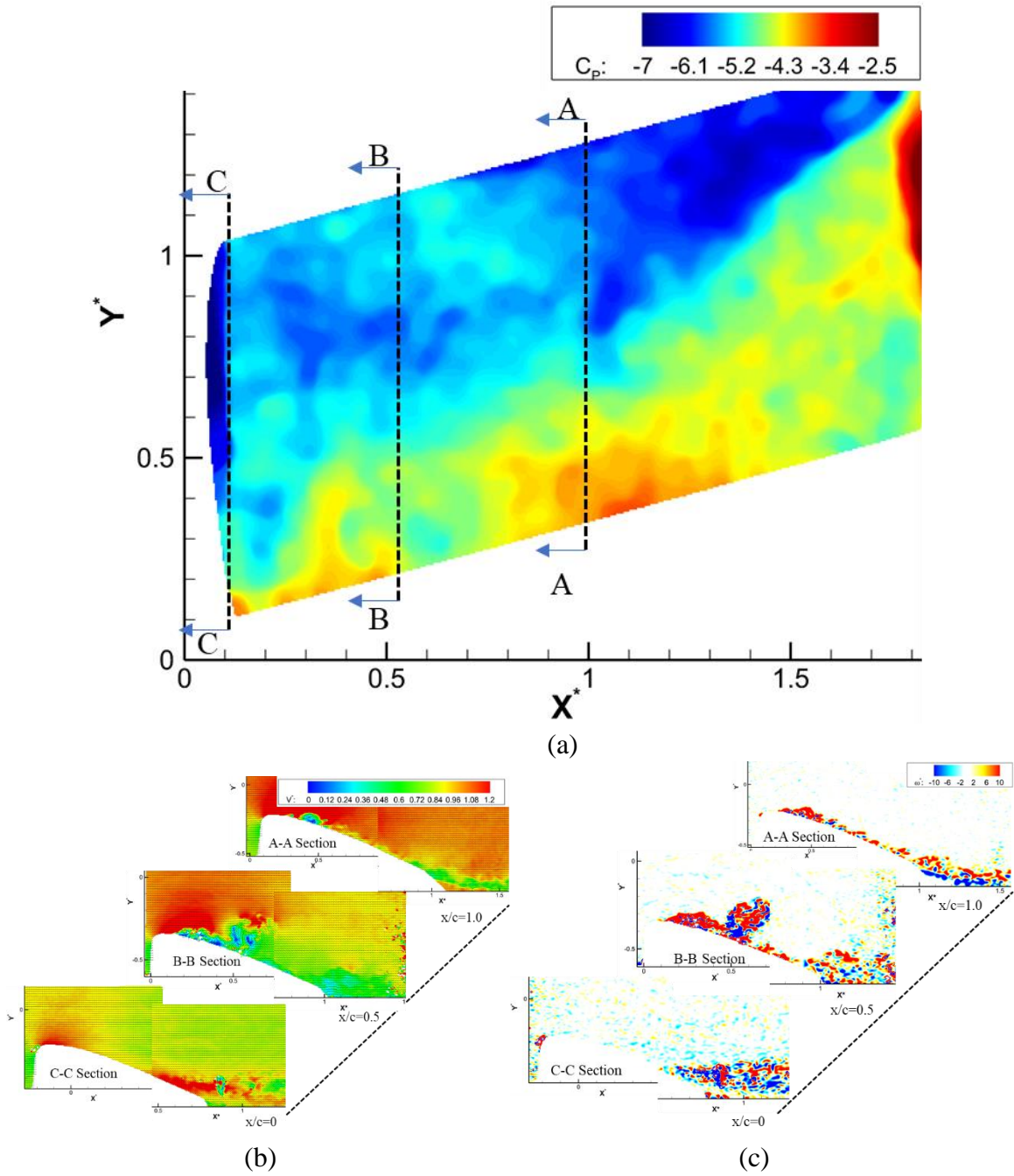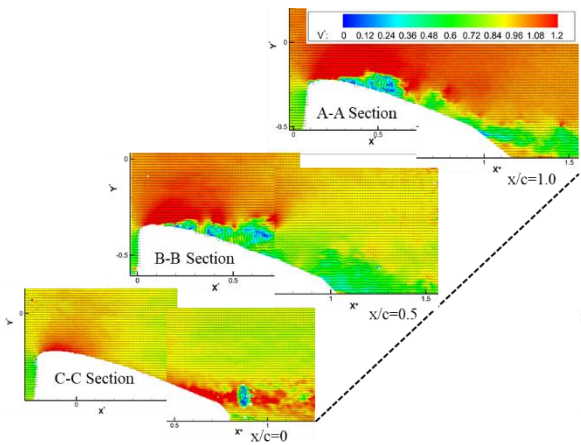

(b)

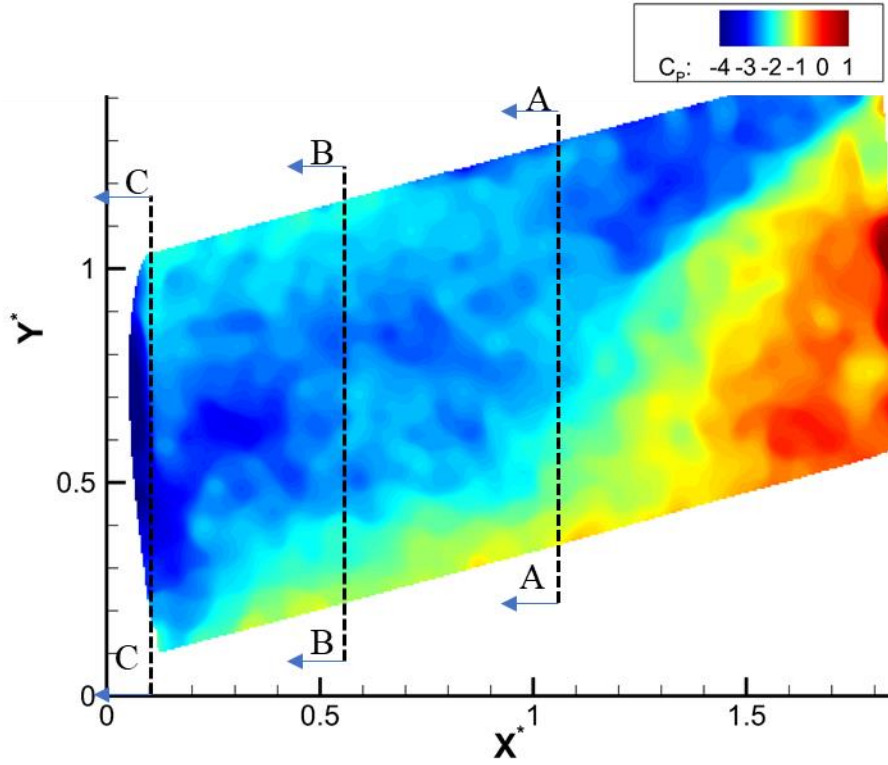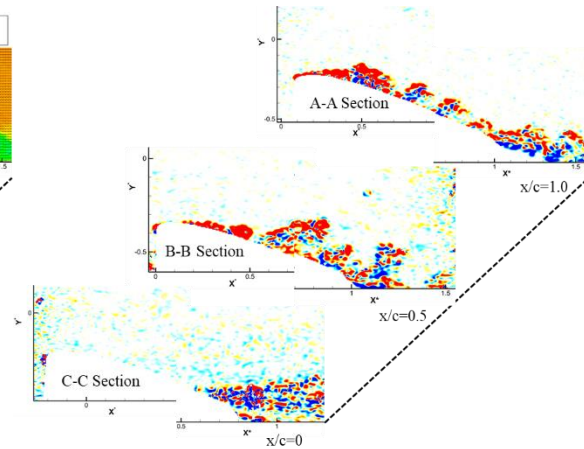

(c)

Figure 47. (a) Instantaneous pressure contour (b) instantaneous velocity map (c) instantaneous vorticity map for phase angle of 21^0 downstroke.
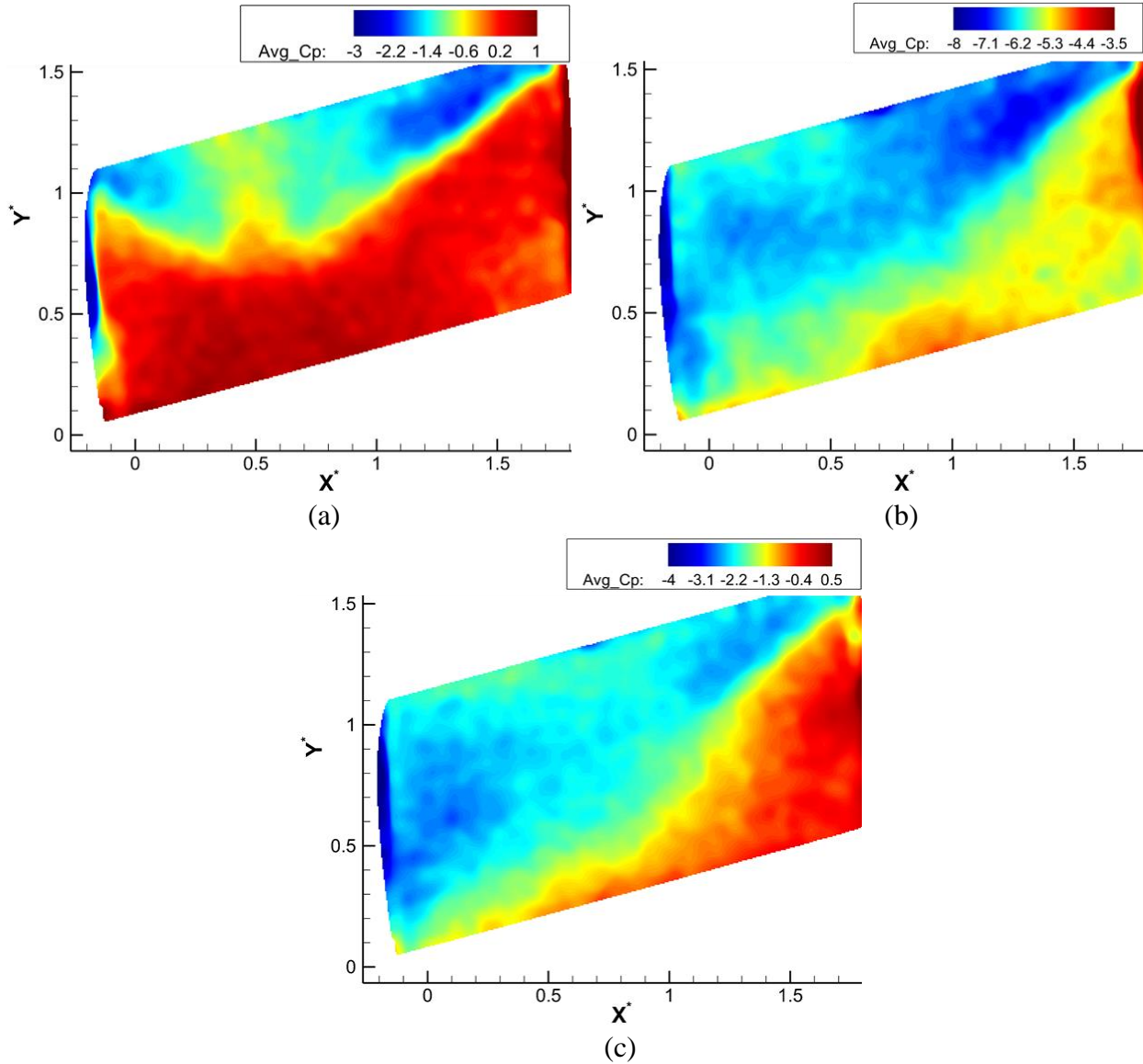
Figure 48. Phase average of pressure map at (a) 21^0 pitching up (b) 22^0 max (c) 21^0 pitching down.

Chapter Conclusion

In this chapter, the experiment was conducted for sweep 15^0 airfoil at Re=2×10^5, and reduced frequency, k=0.2. The data was shown for PIV and PSP experiment. The PIV data shows the separation burst at higher incidence angle during pitching motion of the airfoil. The separation burst indicates the similarity of arch-shaped vortex structure. The PSP results confirms the arch-shaped vortex at phase angle of 21^0 pitching up. At lower reduced frequency less than 0.2, does

not show consistent presence of arch shaped vortex. However, at k=0.2, the pressure distribution on the airfoil surface shows the presence of arch-shaped vortex. The vortex shedding the 2D vorticity and velocity plot indicates the evolution of arch-shaped vortex to a ring-shaped vortex. The finding in this chapters proof the theory conducted by Visbal and Garmann et. al.

CHAPTER 6. CONCLUSION

In this study, the dynamic stall was characterized. The findings show new insight of dynamic stall such as phase coherence, effect of sweep, and proof of the existence of the arch-shaped vortex. The study proves that the dynamic stall vortex in leading edge is aperiodic in nature and the leading-edge of the vortex causes 3-dimensional and uneven pressure distribution on the airfoil surface. The increase of sweep angle causes shift of the dynamic stall vortex towards the outboard of the wing. When the reduced frequency is less then 0.2, the pitching motion does not show any existence of arch-shaped vortex, even the dynamic stall happens. However, when the reduced frequency is equal to 0.2 the moderate sweep airfoil shows the proof of the existence of arch-shaped vortex.

In addition to the present finding, there are some future work that can be done to find the dynamic stall characteristics. One aspect is to change the range of pitching at variable minimum and maximum angles. The present study offers the aspect of dynamic stall characteristics at a fixed minimum and maximum angle. However, the variable range of pitching needs to be investigated. For pitching lower frequency, the reduced range of pitching may cause the instability in boundary layer and eventually the shear layer may roll and deformed to an arch-shaped vortex.

REFERENCES

1. Visbal, M. R., and Garmann, D. J. "Effect of sweep on dynamic stall of a pitching finite-aspect-ratio wing," *AIAA Journal* Vol. 57, No. 8, 2019, pp. 3274-3289.

2. Visbal, M. R., and Shang, J. "Investigation of the flow structure around a rapidly pitching airfoil," *AIAA journal* Vol. 27, No. 8, 1989, pp. 1044-1051.

3. McAlister, K. W., Carr, L. W., and McCroskey, W. J. "Dynamic stall experiments on the NACA 0012 airfoil," 1978.

4. Kuchemann, D., and Weber, J. "The subsonic flow past swept wings at zero lift without and with body." Aeronautical Research Council London (England), 1953.

5. McCroskey, W. J. "Unsteady airfoils," *Annual review of fluid mechanics* Vol. 14, No. 1, 1982, pp. 285-311.

6. Carr, L. W. "Progress in analysis and prediction of dynamic stall," *Journal of aircraft* Vol. 25, No. 1, 1988, pp. 6-17.

7. Ericsson, L., and Reding, J. "Fluid dynamics of unsteady separated flow. Part II. Lifting surfaces," *Progress in Aerospace Sciences* Vol. 24, No. 4, 1987, pp. 249-356.

8. Visbal, M. "On some physical aspects of airfoil dynamic stall," *Proceedings of the International Symposium on Non-Unsteady Fluid Dynamics*. Vol. 92, American Soc. of Mechanical Engineers Fairfield, NJ, 1990, pp. 127-147.

9. Ekaterinaris, J. A., and Platzer, M. F. "Computational prediction of airfoil dynamic stall," *Progress in aerospace sciences* Vol. 33, No. 11-12, 1998, pp. 759-846.

10. Carr, L. W., and Chandrasekhara, M. "Compressibility effects on dynamic stall," *Progress in Aerospace Sciences* Vol. 32, No. 6, 1996, pp. 523-573.

11. Visbal, M. R., and Garmann, D. J. "Dynamic stall of a finite-aspect-ratio wing," *AIAA Journal* Vol. 57, No. 3, 2019, pp. 962-977.

12. Visbal, M. R. "Numerical exploration of flow control for delay of dynamic stall on a pitching airfoil," *32nd AIAA Applied Aerodynamics Conference*. 2014, p. 2044.

13. Visbal, M. R. "Control of dynamic stall on a pitching airfoil using high-frequency actuation," *53rd AIAA Aerospace Sciences Meeting*. 2015, p. 1267.

14. Carlson, B., Ullah, A. H., and Estevadeordal, J. "Experimental Investigation of Vortex-Tube Streamwise-Vorticity Characteristics and Interaction Effects with a Finite-Aspect-Ratio Wing," *Fluids* Vol. 5, No. 3, 2020, p. 122.

15. Tomek, K. L., Ullah, A. H., Fabijanic, C., and Estevadeordal, J. "Experimental Investigation of Dynamic Stall on Pitching Swept Finite-Aspect-Ratio Wings," *AIAA Scitech 2020 Forum*. 2020, p. 1980.

16. Ullah, A. H., Fabijanic, C., Refling, W., and Estevadeordal, J. "Experimental Investigation of the Effect of Sweep on a Pitching Finite-Aspect-Ratio Wing," *AIAA Scitech 2021 Forum*. 2021, p. 1733.

17. Visbal, M. R. "Analysis of the onset of dynamic stall using high-fidelity large-eddy simulations," *52nd Aerospace Sciences Meeting*. 2014, p. 0591.

18. Carta, F., Fink, M., and Jepson, W. "The influence of sweep on the aerodynamic loading of an oscillating NACA 0012 airfoil. Volume 1: Technical report," 1979.

19. Lorber, P., Covino, J., Alfred, And Carta, F. "Dynamic stall experiments on a swept three-dimensional wing in compressible flow," *22nd Fluid Dynamics, Plasma Dynamics and Lasers Conference*. 1991, p. 1795.

20. Henkner, J. "Phenomena of dynamic stall on swept wings," *22nd International Congress of the Aeronautical Sciences, ICAS Paper*. Vol. 2, 2000, p. 2000.

21. Smith, L. R., and Jones, A. R. "Measurements on a yawed rotor blade pitching in reverse flow," *Physical Review Fluids* Vol. 4, No. 3, 2019, p. 034703.

22. Rymarz, P. B., and Ramaprian, B. "Measurements of velocity and vorticity fields around a pitching swept wing," *AIAA journal* Vol. 35, No. 1, 1997, pp. 205-207.

23. Gursul, I., and Cleaver, D. "Plunging oscillations of airfoils and wings: Progress, opportunities, and challenges," *AIAA Journal* Vol. 57, No. 9, 2019, pp. 3648-3665.

24. Chiereghin, N., Cleaver, D., and Gursul, I. "Unsteady force and flow measurements for plunging finite wings," *47th AIAA Fluid Dynamics Conference*. 2017, p. 3127.

25. Visbal, M. R., and Garmann, D. J. "Analysis of dynamic stall on a pitching airfoil using high-fidelity large-eddy simulations," *AIAA Journal* Vol. 56, No. 1, 2018, pp. 46-63.

26. Visbal, M. R., and Benton, S. I. "Exploration of high-frequency control of dynamic stall using large-eddy simulations," *AIAA Journal* Vol. 56, No. 8, 2018, pp. 2974-2991.

27. Rockwood, M., Medina, A., Garmann, D. J., and Visbal, M. R. "Dynamic Stall of a Swept Finite Wing for a Range of Reduced Frequencies," *AIAA Aviation 2019 Forum*. 2019, p. 3335.

28. Liu, T. "Pressure-and Temperature-Sensitive Paints," *Encyclopedia of Aerospace Engineering*, 2010.

29. Wong, O., Watkins, A., and Ingram, J. "Pressure sensitive paint measurements on 15% scale rotor blades in hover," *35th AIAA Fluid Dynamics Conference and Exhibit*. 2005, p. 5008.

30. Gardner, A. D., Klein, C., Sachs, W., Henne, U., Mai, H., and Richter, K. "Investigation of three-dimensional dynamic stall on an airfoil using fast-response pressure-sensitive paint," *Experiments in fluids* Vol. 55, No. 9, 2014, p. 1807.

31. Disotell, K. J., Peng, D., Juliano, T. J., Gregory, J. W., Crafton, J. W., and Komerath, N. M. "Single-shot temperature-and pressure-sensitive paint measurements on an unsteady helicopter blade," *Experiments in Fluids* Vol. 55, No. 2, 2014, p. 1671.

32. Disotell, K. J., Nikoueeyan, P., Naughton, J. W., and Gregory, J. W. "Global surface pressure measurements of static and dynamic stall on a wind turbine airfoil at low Reynolds number," *Experiments in Fluids* Vol. 57, No. 5, 2016, p. 82.

33. Watkins, A. N., Leighty, B. D., Lipford, W. E., Wong, O. D., Oglesby, D. M., and Ingram, J. L. "Development of a pressure sensitive paint system for measuring global surface pressures on rotorcraft blades," *2007 22nd International Congress on Instrumentation in Aerospace Simulation Facilities*. IEEE, 2007, pp. 1-9.

34. Wong, O. D., Watkins, A. N., Goodman, K. Z., Crafton, J., Forlines, A., Goss, L., Gregory, J. W., and Juliano, T. J. "Blade tip pressure measurements using pressure-sensitive paint," *Journal of the American Helicopter Society* Vol. 63, No. 1, 2018, pp. 1-11.

35. Raffel, M., Willert, C. E., Scarano, F., Kähler, C. J., Wereley, S. T., and Kompenhans, J. *Particle image velocimetry: a practical guide*: Springer, 2018.

36. ISSI. "Fast Pressure Sensitive Paints." Vol. 2021 ISSI, https://innssi.com/fast-pressure-sensitive-paints/.

37. Visbal, M. R., and Garmann, D. J. "High-fidelity simulations of dynamic stall over a finite-aspect-ratio wing," *8th AIAA Flow Control Conference*. 2016, p. 4243.